1 **Morphological and optical properties of carbonaceous aerosol particles from ship emissions and biomass burning**

2 **during a summer cruise measurement in the South China Sea**

3 **Cuizhi Sun[1], Yongyun Zhang[1], Baoling Liang[1,&], Min Gao[1], Xi Sun[1,#], Fei Li[1,4], Xue Ni[1], Qibin Sun[1], Hengjia Ou[1], Dexian**

4 **Chen[1], Shengzhen Zhou[1,2,3*], and Jun Zhao[1,2,3*]**

5 [1] School of Atmospheric Sciences, Guangdong Province Key Laboratory for Climate Change and Natural Disaster Studies,

6 and Southern Marine Science and Engineering Guangdong Laboratory (Zhuhai), Sun Yat-sen University, Zhuhai, Guangdong

7 519082, China

8 [2] Guangdong Provincial Observation and Research Station for Climate Environment and Air Quality Change in the Pearl

9 River Estuary, Zhuhai, Guangdong 519082, China

10 [3] Key Laboratory of Tropical Atmosphere-Ocean System, Ministry of Education, Zhuhai, Guangdong 519082, China

11 [4] Xiamen Key Laboratory of Straits Meteorology, Xiamen Meteorological Bureau, Xiamen, Fujian 361012, China

12 [&] Now at Guangzhou Environmental Monitoring Center, Guangzhou, Guangdong 510060, China

13 [#] Now at Centre for Isotope Research (CIO), Energy and Sustainability Research Institute Groningen (ESRIG), University of

14 Groningen, Groningen 9747 AG, the Netherlands

15 *Correspondence to*: Jun Zhao (zhaojun23@mail.sysu.edu.cn) and Shengzhen Zhou (zhoushzh3@mail.sysu.edu.cn)

16 **Abstract.** Carbonaceous aerosols constitute a crucial component of atmospheric marine aerosols among which black carbon

17 (BC) and brown carbon (BrC) are important contributors to light absorption and hence the positive climatic radiative forcing

18 in the marine atmosphere. We conducted a month-long (May 05–June 09, 2021) onboard sample collections and online

19 measurements of carbonaceous aerosols to characterize their morphological and optical properties during a ship cruise in the

20 South China Sea (SCS), covering a marine region of 11.9–24.5 °N and 111.1–118.2 °E. Single particles were collected by a

21 single particle sampler and offline analyses were performed to investigate the mixing state and morphology using a

22 transmission electron microscope (TEM) coupled with energy dispersive X-ray spectroscopy (EDS). Online measurements of

23 BC in $PM_{2.5}$ were made by a seven-wavelength aethalometer and organic carbon (OC)/elemental carbon (EC) mass

24 concentrations were measured by a semi-online OC/EC analyzer. Single particle samples were classified into two modes: "stop"

25 ~~when the ship was anchored and "navigation" when the ship sailed at high speed.~~ Feret diameters of the single particles during

26 navigation and stop showed size distributions with the lognormal fitting peaks at 307 and 325 nm, respectively. The fresh

27 (without coating) and aged BC particles (after removal of coating by the electron beams in TEM) showed ~~comparable~~ same

28 median fractal dimensions (~~1.65 vs 1.66~~1.61), in contrast to their different median lacunarities (0.53 vs 0.59). The aged BC

29 particles showed narrower Feret diameters (~~298~~229 ~~1980~~2557 nm) during navigation than those (~~304~~78 ~~2982~~2926 nm) of

30 freshly-emitted BC from the own ship during stop. Moreover, tar balls, as one important component of single particles from

31 ship emissions and as the tracer of biomass burning, were identified with geometrical diameters of 160–420 nm in the TEM

32 images. The ~~energy dispersive X-ray spectroscopy (EDS)~~EDS analyses showed those tar balls are mainly mixed with sea salt,

33 organics, BC, and sulfate. We also found a significant fraction of aged BC in various mixing states (core-shell, embedded)

34 with other components of the aerosol particles after long-range transport.

35 The campaign was further divided into several periods (before monsoon period, BMP; transition monsoon period, TMP;

36 after monsoon period, AMP; and ship pollution period, SPP) according to the wind direction during monsoon and the own ship

37 pollution. The median OC/EC ratios were 8.14, 5.20, 6.35, and 2.63 during BMP, TMP, AMP, and SPP, respectively, showing

38 higher OC/EC ratios for biomass burning emissions than for fossil fuel emissions. Additionally, the median absorption

39 Angström exponent (AAE) values derived from all wavelengths were 1.14, 1.02, 1.08, and 1.06 for BMP, TMP, AMP and SPP,

40 respectively. Particularly, a median AAE value of 1.93 was obtained during two significant biomass burning events. These

41 results showed that biomass burning (BB) and fossil fuel (FF) combustion contributed to 18–22% and 78–82% of all the BC

42 light absorption without the two intense biomass burning events, during which BB and FF accounted for 42% and 58%,

43 respectively. The two BB events originated from the Philippines and Southeast Asia before and after the summer monsoon.

44 Our results demonstrated that BC can serve as the core of aged particles but the fractal dimensions of BC aggerates were

45 subject to little variation; moreover, such BC particles become much more aggerated after aging in the marine atmosphere,

46 which further affects the light absorption of the BC particles in the SCS. ~~This study provides information about the morphology~~

47 ~~and the optical properties of carbonaceous aerosols which can be used to evaluate their effects on light absorption and hence~~

48 ~~the climatic radiative forcing in the SCS region.~~

49

1 Introduction

Carbonaceous aerosols (e.g., organic carbon (OC), elemental carbon (EC)/black carbon (BC)~~, and brown carbon (BrC)~~)

profoundly impact regional and global climate (Corbin et al., 2019; Lu et al., 2020; Rabha and Saikia, 2020). As an important

component of carbonaceous aerosols, BC can serve as a tracer of anthropogenic pollution once emitted from the incomplete

combustion of fossil fuels and biomass burning. Moreover, BC particles are generally soot-aggerated with ~~onion-like graphite~~

graphene-like layer microstructures which can be observed under electron microscopy (Adachi et al., 2019). BC and EC are

two components of carbonaceous aerosols that are measured differently. BC is typically quantified based on its light-absorbing

properties, while EC is measured using thermal-optical methods (Duarte et al., 2021). However, EC can also be referred to as

graphitic carbon or soot, with some overlap in their definitions. Another important component of carbonaceous aerosols, BrC,

represents a series of light-absorbing organic compounds, contributing significantly to the light absorption of atmospheric

aerosols (Wang et al., 2020b). BrC and BC show different light absorption patterns as a wavelength function. ~~BrC typically~~

~~absorbs more strongly in the visible range (400–700 nm), while BC absorbs more strongly in the ultraviolet (UV) and near-~~

~~infrared (NIR) ranges (200–400 nm and 700–1000 nm, respectively). Therefore,~~ BrC and BC can be distinguished by

measuring the absorption spectra of aerosol particles at different wavelengths (Andreae and Gelencsér, 2006; Bond et al., 2013;

Laskin et al., 2015; Li et al., 2020; Yus-Díez et al., 2021). Tar balls are commonly used as typical tracers of biomass and biofuel

burning due to their composition of amorphous carbon. These particles also belong to BrC ~~due to their light absorption~~

~~properties over a broad range of solar spectra, from around 300 nm in the UV range to 2500 nm in the NIR range~~ because they

are light absorbing organics (Adachi et al., 2019; Hand et al., 2005). Spherical tar balls emitted from biomass burning have

been observed in cases of both wild fire burning (Adachi et al., 2019) and laboratory generated tar ball particles (Tóth et al.,

2014). In the atmosphere, biomass burning produces a significant amount of tar balls, which are not deliquescent but can

absorb water at high relative humidity (RH = ~80%), thereby affecting their ability to scatter and absorb light (Hand et al.,

2005).

The optical properties of BC and BrC particles are affected by several factors including the emission source, coating

component, particle size, morphology, and mixing state of the particles (Wei et al., 2020). The BC configuration in the single

74 particles would influence their radiative effects (Luo et al., 2021). For example, core-shell BC particles show enhanced light

75 absorption compared to bare BC particles, especially when BC particles are coated with absorptive materials such as BrC

76 (Budhavant et al., 2020; Cappa et al., 2012; Shamjad et al., 2012; You et al., 2016). "Lensing effect" refers to the absorption

77 enhancement if BC is coated with non-absorbing organic or inorganic materials (Luo et al., 2021; Yang et al., 2009). In contrast,

78 if the BC coating materials are highly absorptive, no absorption enhancement may occur at shorter visible and UV wavelengths,

79 a phenomenon known as "shielding effect". The shielding and lensing effects depend on the coating thickness over BC (Lack

80 and Cappa, 2010). When BC is well internally mixed with BrC, its total absorption enhancement becomes smaller than the

81 enhancements of not well mixed counterparts due to the absorptive coating that acts as a shield When BC is well internally

82 mixed with BrC, its total absorption enhancement becomes smaller than those of not well mixed counterparts due to the

83 absorptive coating that acts as a shield (Feng et al., 2021). Moreover, it is impossible for BC and other materials to be

84 homogeneously distributed.

85   The extent to which of BC and BrC contribute to light absorption in atmospheric aerosols can be assessed using the

86 absorption Ångstrom exponent (AAE) (Wang et al., 2020a). AAE is a parameter used to quantify the spectral dependence of

87 aerosol light absorption. It is calculated by fitting a power-law relationship between the aerosol absorption and wavelengths

88 over a given spectral range. The AAE is used to identify sources and types of aerosols and a higher AAE value is associated

89 with sources such as biomass burning or urban pollution, while a lower AAE value suggests absorption by larger particles,

90 such as mineral dust or sea salt (Blanco-Donado, 2022; Duarte et al., 2021). However, many factors such as mixing state,

91 coating, particle size, refractive index, wavelength, and emission source, would affect the AAE values for BC and BrC aerosols,

92 leading to large variations among different studies (Moschos et al., 2021). For example, a previous study showed that the AAE

93 values derived from wavelengths of 405 and 781 nm are very sensitive to refractive index and particle diameter (Chylek et al.,

94 2019). The AAE values of 0.8−1.6 at 470 and 950 nm are attributed to traffic emissions and fuel combustion (Ezani et al.,

95 2021). Comparatively, those AAE values can be as large as 2.0 for ship emissions (Helin et al., 2021). Moreover, the

96 recommended AAE value for fossil fuel (FF) and biomass burning (BB) is 1 and 2 (or higher), respectively (Liu et al., 2023).

97 Other AAE values were also found in previous studies for FF (0.9) and BB (1.68) (Zotter et al., 2017) or FF (1.2) and BB (2.2)

98 as the mostly used optical pair (Milinković et al., 2021). The AAE values of 1.4 and 1.7 for BC and BrC were set to be the

99   lower and upper limits in the modelling study of biomass burning particles mixed with BC and BrC (Chylek et al., 2019).

100   However, the use of constant AAE values for calculating the BC fractions from BB and FF led to large uncertainties without

101   knowledge of the core size or coating thickness of the BC particles (Virkkula, 2021). Currently, the effect of the light absorption

102   is not well known for the carbonaceous particles in the marine atmosphere due to scarce ship-based measurements.

103   The optical properties of BC and BrC particles can also be investigated through fractal dimension (D_f) analysis based on the

104   fractal properties of BC aggerates. D_f illustrates how particles aggregate and grow and it can be determined through boxing

105   counting calculation, ensemble method, or soot parameter method with TEM images (Pang et al., 2022). The D_f values are

106   mainly related to emission sources and aging process of the particles. Previous studies showed that the D_f values of fresh BC

107   particles tend to be small but become larger after aging because the particles are more compact due to coatings (Luo et al.,

108   2022; Wang et al., 2017). D_f values of 1.8 and 2.6 were used respectively for fluffy and compact BC particles in a numerical

109   study to investigate the impact of the BC morphology on light absorption (Luo et al., 2021). Laboratory experiments simulating

110   wildfires showed that the D_f values of freshly emitted BC were in a range of 1.74−1.92 (Chakrabarty et al., 2006), compared

111   to the range of 1.67−1.83 from a field study of the Las Conchas fire (China et al., 2013). A similar range of the D_f values of

112   1.67−1.93 were found at a remote site in the southeastern Tibetan Plateau (Wang et al., 2017). The obtained D_f values for the

113   traffic emissions were as large as 3 (Wei et al., 2020). In addition to the emission sources and aging process, D_f is also dependent

114   on the particle size. A previous experimental study found that for polystyrene latexes (PSL) particles, the D_f values decreased

115   with the increase of particle size up to 200 nm (Wu et al., 2013b). Nevertheless, knowledge of the fractal dimension for

116   carbonaceous particles in the marine atmosphere is currently very limited, hindering our ability to understand the aging process

117   and the optical properties of these particles.

118   In the past years, carbonaceous aerosols in the marine atmosphere have been extensively studied on regional and global

119   scales, focusing on the transport of anthropogenic emissions to the sea areas. The BC background concentrations in Antarctic

120   and Arctic regions are below 20 ng m^{-3} (Fossum et al., 2022). The BC outflows from Asia to the Pacific Ocean exhibit seasonal

121   variations and originate from anthropogenic and biomass-burning sources in China, Siberia, and Southeast Asia (Matsui et al.,

122   2013). Ship-based BC and EC measurements reveal significant influence of continental transport on remote oceanic regions,

123   including the Bay of Bengal (Kedia et al., 2012), Indian Ocean (Kompalli et al., 2021), Southern Indian Ocean and the Southern

124   Ocean (Ueda et al., 2018), North Sea (Bencs et al., 2020), Antarctic (Chaubey et al., 2013; Schmale et al., 2019), North Pacific

125   (Taketani et al., 2016; Xing et al., 2014), Arctic (Pankratova et al., 2021; Sharma et al., 2019), Northeast Atlantic (Fossum et

126   al., 2022), the Yellow Sea (Kwak et al., 2022), and Western Pacific (Ma et al., 2022). However, to our knowledge, the BC mass

127   concentrations have been found to vary significantly across different oceans and seasons, with levels from 3 to 2800 ng m^{-3}

128   and being influenced by anthropogenic activities and seasonal factors. The online BC measurements in the South China Sea

129   (SCS) region are limited. An early study reported BC concentrations on Yongxing Island during the rainy season (May 16–

130   June 20, 2008) and the dry season (Dec. 12, 2008–Jan. 8, 2009), with average concentrations of 0.54 and 0.67 µg m^{-3},

131   respectively (Wu et al., 2013a). Recent studies conducted at coastal sites in the SCS found that BC concentrations are strongly

132   impacted by the land anthropogenic emissions (Wang et al., 2022). The time-resolved BC concentration varies with the vertical

133   heights (Sun et al., 2020c) and the carbonaceous materials of OC and EC account for 31–62% in PM$_{2.5}$ (Yan et al., 2018).

134   Nevertheless, quantification of the light absorption potential of BC and BrC aerosols remains challenging due to the limited

135   knowledge regarding the morphology, particle size, and mixing state of carbonaceous particles in the SCS (Kompalli et al.,

136   2021). Furthermore, the atmosphere in the SCS is typically influenced by the southwesterly monsoon from May to August

137   (Wang and Wu, 2020), which affects the air masses from Southeast Asia. In this study, we conducted ship-based measurements

138   of BC, OC/EC, and single particle sampling during summer (May 05–June 09, 2021) in the SCS. The morphology (i.e., the

139   fractal dimension and the size of the single BC particles) and light absorption properties of carbonaceous particles were

140   characterized. The source origins, relationships between the D_f and BC size, as well as the impact of summer monsoon on the

141   light absorption of the BC particles are discussed.

142   **2 Methods**

143   **2.1 Cruise route and instrumentation**

144   The cruise measurements were carried out from May 5 to June 9, 2021, covering a marine area of 11.9–24.5 °N and 111.1–

145   118.2 °E in the SCS. Single particles were collected on the TEM grids (3.05 mm I.D., copper meshed and covered with lacey

146   carbon film) located on the front deck during ship navigation and stop using a single-stage particle sampler (DKL-2, Genstar

147 Electronic Technology Co., Ltd., China) which is the same as other studies (Liu et al., 2021; Pang et al., 2022). The sampling

148 flow rate and time were set at 1 L min^{-1} and 10 min, respectively, for each collection. The nozzle diameter of this single-cascade

149 impactor is 0.3 mm. The particles with aerodynamic diameters above 0.2 μm were collected with a collection efficiency of

150 50%, assuming a particle density of 1.5 kg m^{-3} (Marple and Olson, 2011). More details can be found in the supplementary

151 information (Section 1 of SI). The mixing state and morphology of the single particles were analyzed utilizing a transmission

152 electron microscope (TEM, FEI Tecnai G2 Spirit, Holland) operated at an accelerating voltage of 120 kV, in conjunction with

153 an energy dispersive spectrometer (EDS, Bruker Nano GmbH Berlin, Esprit 1.9, Germany) for elemental analysis. The

154 thickness of the EDS detector (type XFlash 5060) is 0.45 mm with a Si dead layer of 0.029 mm. Notably, in the EDS spectra,

155 when analyzing particle composition, Cu should be excluded, and a considerable level of C and Si should be observed in the

156 background signals due to the presence of Si in the detector, Cu and C in the TEM grid. The substrate holder of TEM was tilted

157 25° for thorough inspection during imaging and EDS analysis.

158 The sampling inlets were installed on the bow of the research vessel with a height of ~ 15 m above sea level. The own ship

159 emissions (e.g., engine, cooking, etc.) were exhausted from the chimney on the stern with a linear distance of ~ 22 m to the

160 inlets. The BC mass concentrations were measured by an aethalometer (Model AE33, Magee Scientific, USA) with a ~~high~~

161 time resolution of ~~one second or~~ one minute (Drinovec et al., 2015). Note that the BC mass concentrations derived from AE33

162 are referred to as equivalent BC mass concentrations due to the light absorption of both BC and BrC at 880 nm. The sampling

163 air was regulated by a PM$_{2.5}$ cyclone (BGI Inc., Waltham, MA, USA) and subsequently dried by a Nafion dryer (Model MD-

164 700 series, Perma Pure Inc., USA) with a relative humidity below 40% through the filter tape (type 8060) at a flow rate of 5 L

165 min^{-1}. Data corrections were made for the employed Aethalometer AE33, considering the multiple scattering parameters

166 (C(λ)=1.39) for the used filter type, the leakage factor (ζ=0.01), and the compensation parameters (K$_{min}$=-0.005, K$_{max}$=0.015).

167 ~~The optical attenuation (ATN) was measured simultaneously from the two spots on the filter.~~ The measured attenuation at

168 seven wavelengths (7 channels) is used to determine the wavelength-dependent absorption coefficient. The mass specific

169 absorption cross-sections (MAC, σ$_{air}$) applied in the BC calculations were 18.47, 14.54, 13.14, 11.58, 10.35, 7.77, and 7.19 m^2

170 g^{-1} for wavelengths of 370, 470, 520, 590, 660, 880, and 950 nm, respectively (Ausmeel et al., 2020). The measured values at

171 880 nm (channel 6) are for black carbon concentration calculation, and at 370 nm (channel 1) for UV particulate matter (UVPM)

7

172   concentration (Drinovec et al., 2015). The detection limit of AE33 aethalometer is approximately 0.03 µg m^{-3} for 1-min

173   integration period and below 0.005 µg m^{-3} for 1-hour integration period. The instrument was automatically calibrated by zero

174   air every day. Notably, significant spikes were observed during periods when the ship was stationary, when it was travelling at

175   low speeds, and when the wind was blowing from the stern of the vessel.

176   The OC/EC concentrations were measured by a semi-continuous OC/EC analyzer (Model-4, Sunset Laboratory Inc., USA)

177   based on the optical attenuation and thermo-optical transmittance methods (Geron, 2009) under the NIOSH 5040 thermal-

178   optical protocol (Lappi and Ristimaki, 2017). Similarly, the sampling air passed through a PM$_{2.5}$ cyclone (BGI Inc., Waltham,

179   MA, USA) and was dried by a Nafion dryer (Model MD-700 series, Perma Pure Inc., USA) with a relative humidity below

180   40% at a flow rate of 8 L min^{-1}. The air then passed through a denuder for the removal of volatile organic compounds (VOCs)

181   and the particles were collected on the quartz filter with 45-min accumulation and 15-min analysis. The instrument was

182   calibrated with the standard sucrose solution as recommended. The manufacturer-claimed detection limits are 0.4 and 0.2 µg

183   m^{-3} for OC and EC, respectively (Brown et al., 2019). However, several previous studies showed that these values may vary

184   substantially in a range of 0.04−2 and 0.001−0.5 µg m^{-3} for OC and EC, respectively, due to the artifact of the quartz filters

185   (Bao et al., 2021; Bauer et al., 2012; Chen et al., 2017; Jung et al., 2011; Karanasiou et al., 2020; Park et al., 2018; Zhang et

186   al., 2021). Here, we estimated the detection limits of 0.15 and 0.012 µg m^{-3} for OC and EC based on 26 effective blank

187   measurements with 3 times standard deviation (3σ) during the campaign. The limit of detection (LOD) for OC and EC is 0.18

188   and 0.19 µg m^{-3}, respectively, calculated as three times the standard deviation of replicate measurements of a standard sucrose

189   solution with a carbon content of 10.516 µg m^{-3}. The Sunset OC/EC analyzer also measures optical EC based on the

190   transmission of 660 nm wavelength light through the quartz fiber filter employed for sampling, similar to the AE33 for optical

191   BC measurements. Optical EC is defined as the apparent EC on the filter based on the measured apparent absorbance and the

192   fixed absorption coefficient according to the user's manual of the Sunset OC/EC. Both our study and a previous study (Brown

193   et al., 2019) showed that the optical EC concentrations from Sunset were comparable with the BC concentrations from AE33.

194   Note that the resultant optical EC concentrations from the instrument output may be overestimated due to the limitation of the

195   filter-based optical measurements.

196

197   The measurements of solar radiation (SR), temperature (T), pressure (P), relative humidity (RH), relative wind direction

198   (RWD), and relative wind speed (RWS) were provided by the automatic weather station (AWS430, Vaisala Inc., Finland) (Song

199   et al., 2022) equipped on the front deck of the research vessel. This station comprises a range of integrated sensors, including

200   a wind speed and direction sensor (model WMT702), a temperature and humidity sensor (model HMP155), and an atmospheric

201   pressure sensor (model BARO-1). The cruise route for ship navigation is from the global positioning system (GPS) onboard

202   the ship (Seapath 330+, Kongsberg Inc., Norway). ~~equipped on the research vessel. The cruise route is from the global~~

203   ~~positioning system (GPS) onboard the ship.~~

204   **2.2 Data analyses and processing**

205   ~~2.2 Data analyses and processing~~

206   **2.2.1 Analyses of single particles**

207   A total of 34 samples (15 during navigation and 19 at stop) were analyzed and more than 20 bright-field TEM images were

208   randomly captured for each sample except for those at the center of the grids where particles were easily overlapped. A total

209   of 15624 single particles were statistically analyzed to obtain morphology information (i.e., the Feret diameter, area, perimeter)

210   for each particle using the software Image-J (1.53q, National Institute of Health, USA) (Cheng et al., 2021). In the analysis of

211   particle size, the Feret diameter is defined as the distance between the parallel tangential lines that constrain the particle

212   perpendicularly. In this study, we applied the Feret diameter as the longest distance between any two points along the boundary

213   of the selected particles. Moreover, we utilized "geometrical diameter" to describe the size of tar balls with circular shape,

214   which signifies the distance between two points located on the surface of a geometric shape, with this line passing through the

215   shape's center. Using "Geometrical diameter" is suitable to quantify the size of the observed tar balls which excluded any

216   coatings or additional materials. Specifically, we employed TEM data acquisition software to measure the geometrical

217   diameters of observed tar balls. The D_f values of the BC particles were estimated using the boxing counting method using the

218   plugin Fraclac. An example was given in the SI (section 2, Fig. S1) to show how to calculate D_f using the software. A detailed

219   description of the procedure using the boxing counting method and the software ImageJ can be found in the SI. The D_f values

220   are very sensitive to the fill extent and sizes of the particles. A previous study showed low fractal dimensions when the particles

221   contain void volumes (Peyronel et al., 2010).

222   The own ship emissions can be identified using various measures, for example, high CO, NO_x concentrations (Sun et al.,

223   2020b), high BC concentrations (Alroe et al., 2019; Shank et al., 2012), regular cooking emissions (Cai et al., 2020), and wind

224   speeds/directions between the ship stop and start operation (Ausmeel et al., 2020; Kwak et al., 2022). The contribution of ship

225   emissions to BC sources on the marine atmosphere depends on engine types, operation modes, fuel types, and loadings (Gagne

226   et al., 2021; Jiang et al., 2018; Karjalainen et al., 2022; Lack and Corbett, 2012; Wu et al., 2021; Zhao et al., 2020). Here, we

227   classify two sampling modes (navigation vs stop) of single particle analyses according to ship operation, and relative wind

228   direction/speed. In this study, the relative wind direction/speed is relative to the ship heading. The navigation mode is

229   constrained by the relative wind direction of 0–80° or 280–360°, and the relative wind speed greater than 5 m s^{-1}, averaged

230   for every 10 minutes (consistent with the collection time of TEM samples). The stop mode is set with the relative wind direction

231   of greater than 80° and less than 280°, or the relative wind speed lower than 5 m s^{-1}. The navigation mode samples are mainly

232   from marine air and air masses of long-range transport while the stop mode collected air masses which are mixed with the own

233   ship emissions. The wind direction (speed) and relative wind direction (speed) are calculated by Eq. (1) (Aijjou et al., 2020).

234 $$V_R = \sqrt{V_s^2 + V_w^2 + 2 * V_s * V_w * \cos\alpha} \tag{1}$$

235   where V_R is the relative wind direction (speed), V_s is the ship direction (speed), V_w is the true wind direction (speed), α is the

236   angle between the ship heading and the true wind direction.

237   The temporal profiles of ship heading directions, and relative wind direction/speed are shown in the SI (section 3, Fig. S2).

238   Details of the two sampling modes (navigation vs stop) on a vector average of 10 minutes are listed in Table S1 and Fig. S3.

239   Here, we distinguished the own ship emissions (research vessel) from those of other ships or long-range transport based on

240   the following criteria: low relative wind speed (< 5 m s^{-1}), relative wind direction encompassing ship exhaust (80–280°), and

241   a substantial AE33-derived hourly averaged BC mass concentration (>2 µg m^{-3}). Other ship emissions far from the research

242   vessel are treated as a part of the transported air masses in this study.

243 ~~Here, we distinguished the own ship emissions (ship pollution) from those of other ships or from long-range transport.~~

244 ~~In addition, an hourly averaged BC concentration above 2 μg m⁻³ was also considered as ship pollution based on the~~

245 ~~time series of BC concentration without significant interference of self-emission.~~

246 2.2.2 BC, OC, EC and optical EC data

247 In this study, BC data obtained from the AE33 instrument are referred to as BC, while data from the OC/EC analyzer is

248 expressed as thermal OC, thermal EC, and optical EC. Here, we averaged the BC mass concentrations over one minute and

249 excluded those below the detection limit of 0.03 μg m⁻³ ~~for~~ to minimizing the variations. We also removed the own ship

250 emissions which are characterized by spikes in particle number concentrations according to the wind directions (Fossum et al.,

251 2022). BC mass concentration was calculated using Eqs. (2, 3) which are cited from the AE33 aethalometer user's manual (Ver

252 1.54).

253 $$ATN = -100 * \ln (I/I_0) \hspace{3cm} (2)$$

254 where ATN is optical attenuation, I_0 is reference signal, I is spot signal.

255 $$BC = \frac{S*(\Delta ATN_1/100)}{F_1(1-\zeta)*\sigma_{air}*C*(1-k*ANT_1)*\Delta t} \hspace{2cm} (3)$$

256 where BC is black carbon concentration, S is spot area, F_1 is measured flow, ζ is leakage factor, σ_{air} is the mass absorption

257 cross-section (MAC), C is multiple scattering parameter, k is compensation parameter, and t is time.

258 AAE was calculated according to Eq. (~~1~~4) using the light absorption at wavelengths of 470 and 950 nm, which are built-in

259 algorithms in the AE33 aethalometer as described elsewhere (Helin et al., 2021; Kang et al., 2022; Milinković et al., 2021;

260 Zotter et al., 2017). This method serves as a two-composition source apportionment for BC emitted from fossil fuels and

261 biomass burning (AAE model).

262 , which applied AAE=1 for fossil fuel and AAE=2 for biomass. The calculations for BC(BB) and BC(FF) are shown in Eqs.

263 (5–7) which are referred to the AE33 aethalometer user's manual and publication (Sandradewi et al., 2008). The optical

264 absorption coefficient is the sum of biomass burning and fossil fuel burning contributions. Basic equations are using Beer-

265 Lambert's Law.

$$266 \quad \mathrm{AAE} = -\frac{\ln\frac{\sigma_{abs}(\lambda_1)}{\sigma_{abs}(\lambda_2)}}{\ln\frac{\lambda_1}{\lambda_2}} \tag{4}$$

267 where σ_{abs} is aerosol absorption coefficient, σ_{air} is mass absorption cross-section (MAC), $\sigma_{abs} = BC*\sigma_{air}$. $\lambda_1 = 470$ nm and $\lambda_2 =$

268 950 nm.

$$269 \quad \frac{\sigma_{abs}(470\ nm)_{FF}}{\sigma_{abs}(950\ nm)_{FF}} = \left(\frac{470}{950}\right)^{-AAE_{FF}} \tag{5}$$

$$270 \quad \frac{\sigma_{abs}(470\ nm)_{BB}}{\sigma_{abs}(950\ nm)_{BB}} = \left(\frac{470}{950}\right)^{-AAE_{BB}} \tag{6}$$

$$271 \quad \sigma_{abs}(\lambda) = \sigma_{abs}(\lambda)_{FF} + \sigma_{abs}(\lambda)_{BB} \tag{7}$$

272 where $\sigma_{abs}(470\ nm)_{FF}$ and $\sigma_{abs}(950\ nm)_{FF}$ are the aerosol absorption coefficients at wavelengths of 470 and 950 nm for fossil

273 fuel (FF), $\sigma_{abs}(470\ nm)_{BB}$ and $\sigma_{abs}(950\ nm)_{BB}$ are the aerosol absorption coefficients at wavelengths of 470 and 950 nm for

274 biomass burning (BB), AAE_{FF} and AAE_{BB} are equals to 1 and 2, respectively.

275

$$276 \quad \mathrm{AAE} = -\frac{\ln\frac{\sigma_{ap}(\lambda_1)}{\sigma_{ap}(\lambda_2)}}{\ln\frac{\lambda_1}{\lambda_2}} \tag{1}$$

277 where σ_{ap} is the aerosol absorption coefficient, $\sigma_{ap} = BC*MAC$. $\lambda_1 = 470$ nm and $\lambda_2 = 950$ nm.

278 Alternatively, AAE can be obtained from the negative slope of linear regression between the log-transformed $\sigma_{abs}$$\sigma_{ap}$ and all

279 the wavelength spectra so that hourly AAE values (all λ) can be obtained following a similar method in Retama et al. (2022).

280 Details are shown in the SI (Section 4, Figure S4). Here, we define Delta-C as the difference between the concentration derived

281 from the aforementioned UVPM data (at 370 nm) and BC concentration (at 880 nm). This Delta-C parameter was employed

282 as an indicator of smoke from biomass burning in previous wood biomass burning studies (Harrison, 2020; Zhang et al., 2017).

283 The OC and EC (thermal) concentrations lower than the detection limits (0.15 and 0.012 μg m^{-3} for OC and EC, respectively)

284 were excluded. Additional data were removed for those with laser correction factors below 0.88 and calibration peak areas

285 lower than the initial calibration levels (within 10%), and a total of 550 551 h data were used for further analysis. In comparison,

286 the Sunset optical EC (at 660 nm) is generally consistent with the Magee AE33 aethalometer derived BC (at 880 nm) within

287 9% (Brown et al., 2019) which is shown in Section 3.3. The EC concentration data from Sunset were considered as ship

12

288 pollution and were discarded when the BC concentrations from the AE33 aethalometer were higher than 2 μg m^{-3}, in addition

289 to those with relative wind directions of 80–280° regardless of the BC concentrations as mentioned before.

2.2.3 HYSPLIT backward trajectory and MODIS fire data

291 The backward trajectories were calculated using NOAA HYSPLIT (Hybrid Single-Particle Lagrangian Integrated Trajectory)

292 (Version 5) at heights of 100, 500 and 1000 m above ~~the~~ sea level (AGL). Daily meteorological data with 1.0°×1.0° spatial

293 resolution for trajectory calculation were downloaded from the global data assimilation system (GADS)

294 (ftp://arlftp.arlhq.noaa.gov/pub/archives/gdas1/). Here, we calculated the 72-h back trajectories of air masses arriving at the

295 single particle~~s~~ sampling sites along the cruise route.

296 Moderate Resolution Imaging Spectrometer (MODIS) data are available from the Near real-time MODIS Collection 6

297 products (https://firms.modaps.eosdis.nasa.gov/download/). Here, we selected a region of 102–127 °E and 0–30 °N fully

298 covering the campaign area. The number of fire hotspots was counted each day during the campaign with a confidence level

299 of higher or equal to 80% as recommended (Giglio et al., 2020). ~~Detailed~~ A detailed description of the fire detection algorithms

300 is available online (https://earthdata.nasa.gov/what-is-new-collection-6-modis-active-fire-data).

3 Results and discussion

3.1 Overview

303 Figure 1 shows the time series of ship cruise route and the single particle sampling locations during ship navigation (marked

304 as solid triangles) and stop (marked as open squares) over the SCS during the campaign. The cruise sequences are AB→C→

305 D→EB→D→A, with AB and EB being non-stop cruise, otherwise the ship stopped occasionally along the arrow routes for

306 other research tasks. Figure 2 shows the time series of the meteorological variables (i.e., solar radiation (SR), temperature,

307 pressure, relative humidity (RH), wind direction (WD), and wind speed (~~WS~~WS)) during the whole campaign (May 05–June

308 09, 2021). The measurements were conducted mostly ~~under~~ on sunny days prior to June 02 as shown by the SR data.

309 Subsequently, it became rainy and cloudy due to the summer monsoon in the SCS. One notable meteorological feature during

13

310 the campaign was the occurrence of the summer monsoon starting from May 27 close to the site *E*, during which (May 27–

311 June 01), an increase of RH (~9% from campaign-averaged 78.7% to monsoon period-averaged 85.6%) and a slight decrease

312 of pressure (~0.2% from 1007.4 to 1005.4 hPa) were observed. Meanwhile, the wind directions were mainly southerly during

313 this period and later changed to southwest.

314 It should be noted that Typhoon 202103 (CHOI-WAN) travelled across B→D, resulting in a bulge in the middle of the

315 cruise route ~~for avoiding~~to avoid the typhoon during June 03–05, 2021. The typhoon track is available online with the last

316 accessed date Mar. 25, 2023: http://agora.ex.nii.ac.jp/digital-typhoon/summary/wnp/s/202103.html.en. The typhoon was

317 initiated at 02:00 local time on May 31 and dissipated at 14:00 on June 05, 2021 (Figure S5). It passed over our cruise route

318 from June 03 to June 05, 2021. While no significant increase of absolute wind speed was seen in Figure 2, a significant increase

319 of relative wind speed was shown in Figure S2, along with an obvious decrease of atmospheric pressure during the typhoon

320 period (Figure S5). The measured relative humidity increased from May 27 to June 01, prior to the presence of the typhoon,

321 which can be attributed to the decrease of ambient temperature during this period.

322 Figure 3 shows the time series of the mass concentrations of carbonaceous aerosol components in $PM_{2.5}$ (i.e., BC, UVPM,

323 OC, and EC) during the whole campaign. Frequently high spikes of the mass concentrations of carbonaceous aerosol

324 components were observed due to the ship pollution from the research vessel. We notice that ship pollution was significantly

325 pronounced on the first two days after the ship left the harbor and on the last 3–4 days before the ship returned to the harbor,

326 during which the spikes of BC and UVPM concentrations were measured by the Magee AE33 aethalometer with the relative

327 wind direction of 80–280°. Before May 08 and after June 05, higher UVPM, OC, and EC concentrations were observed, which

328 can be attributed to significant fresh ship emissions from the research vessel, as evidenced by simultaneous higher BC

329 concentrations. Similar spikes in BC concentrations were observed during other measurement periods, either preceding or

330 following the monsoon period, which were caused by emissions from the frequent stops and starts of the ship. Note that no

331 significant diurnal trend for OC was observed during those aforementioned periods.

332 Figure 4 shows the time series of fire spots distribution and the 72-h backward trajectories at three AGLs (100, 500 and

333 1000 m) over the SCS during the campaign. Only several backward trajectories are shown to avoid massive overlapping.

334 Several fire spots located in the sea were attributed to oil or natural gas drilling processes which generate thermal energy,

combustion, and exhaust. Such processes included the prevalent hydrocarbon exploration and production activities in this region. A comprehensive cartographic representation of these endeavors within the SCS can be accessed via the online platforms (https://amti.csis.org/south-china-sea-energy-exploration-and-development/). Note that since the ship moved along the cruise route, the air mass backward trajectories also changed with the movement of the ship. For example, significant biomass burning was detected in Laos, northern Vietnam, and the Philippines during May 15–24, as indicated by the corresponding fire spots. However, the back trajectories to the sampling route (C→D) during this period were mainly from the Philippines.

Here, we classified the campaign period into several groups based on the cruise route, change of wind direction during monsoon, backward trajectories, and ship pollution, as listed in Table 1: (1) BMP-1 (before monsoon period 1), AB route mainly with northeast wind direction during May 05–09; (2) BMP-2, B→C→D route close to the Philippines primarily with southeast wind direction during May 10–22; (3) BMP-3, D→E close to mainland China with the same wind direction as BMP-2 during May 23–26; (4) TMP (transition monsoon period), EB route with south wind direction during May 27–Jun 01; (5) AMP (after monsoon period), B→D→A route with southwest wind direction during June 02–09; (6) SPP (ship pollution period), ~35% of the online measurement data could be attributed to this category in this study due to the interference from the research vessel own emissions.

3.2 Single particle analysis of BC and tar balls

Particle size distribution, composition, and size-dependent BC fractals were investigated based on TEM images. The Feret diameter is commonly used in microscopy for particle size analysis (Zefirov et al., 2018). The size distribution of all the single particles from the analyzed TEM images is depicted in Fig. 4 Fig. 5. The distribution is represented with histograms starting at 50 nm, a width interval of 20 nm, and a bin number of 200. The choice of bin width may vary depending on cases but it is close to the quotient value of the square root of the measured particle number divided by the overall width of the distribution (Pabst and Gregorova, 2007). Moreover, lognormal fitting is used for the peak size identification of particle size distribution (Rice et al., 2013). Figure 5aFigure 4a shows a fitted peak Feret diameter of 307 nm for a total of 6613 particles from 15 samples during navigation, while a fitted peak Feret diameter of 325 nm was obtained for a total of 9011 particles from 19

359   samples during stop (Fig. 5b~~Fig. 4b~~). Note that we could not successfully obtain a bimodal or multi-peak fit for the data of the

360   stop cases using multi-peak fitting function in the Igor Pro software, as shown in Figure S6. Hence, we believe that single peak

361   fitting best described the distribution in our stop cases, as illustrated in Figure 5. Particles collected during navigation were

362   predominantly aged at high wind speeds, while particles during stop were mixed significantly with freshly emitted particles

363   from the own ship and from other merchant ships or those from long-range transport, possibly leading to the variation of the

364   size distribution. Although the bimodal distribution was observed from particles in the indoor air, which was likely caused by

365   fresh emissions and secondary formation (Pipal et al., 2021), we did not obtain significant bimodal peaks for both navigation

366   and stop particles.

367   We obtained characteristic values for the particle shape descriptors such as circularity (0.7 ± 0.2) and aspect ratio (1.2 ± 0.3)

368   for all the particles collected during navigation and stop, implying that these particles are not perfectly spherical and may vary

369   in their mixing states. Figure 6~~Figure 5~~ (top images) shows a comparison of the mixing states during navigation (a-c) and stop

370   (d-f) from typical BC TEM images. The BC particles collected during navigation are in the embedded (a), external (b), or core-

371   shell (c) mixing states classified with the methods which are based on single particle analysis of island and mountain samples

372   across East China Sea and Japan (Adachi et al., 2014; Sun et al., 2020a). More TEM images for the heavily coated internal

373   and external BC particles from navigation can be found in the SI (section 4~~7~~, Fig. S7~~Fig. S3~~). The EDS analysis showed that

374   the single particles during navigation were predominantly composed of carbon (C), oxygen (O), sulfur (S), potassium (K),

375   sodium (Na), chloride (Cl), magnesium (Mg), and calcium (Ca) (Fig. S8~~Fig. S4~~), indicating that those BC particles were coated

376   with sulfate, sea salt, and organics. Furthermore, small externally mixed BC particles can be transported over the sea and easily

377   coated during long-range transport. Under the TEM electron beam, these coated volatile components were easily vaporized to

378   expose the BC fractal frame (Fig. S7d-f~~Fig. S3d-f~~).

379   Comparatively, a mixture of aged BC particles and much larger fresh BC particles as well as smaller scattered BC particles

380   during stop were found (Fig. 6d-f), which were likely emitted from other ships (Fig. 6d) and the research vessel (e, f). These

381   TEM images showed that the compressed BC particles are typically more aged and atmospherically processed, while the fractal

382   BC particles are fresh. Moreover, EDS analysis showed that sulfate formed from aqueous processes and less viscous organic

383   coating indicate an aging process. Those BC particles with Feret diameters larger than 2 µm during stop were fractal aggerates

which could unlikely survive due to deposition during long-range transport. In addition, heavily coated internal BC particles were found during stop due to the mixing between ship pollution and the marine air (Fig. S9). Moreover, such particles could also be condensation of organics during the cooling process after they were emitted from the ship engine. ~~Comparatively, much larger BC particles as well as smaller scattered BC particles during stop were found (Fig. 5d-f), among which were apparently emitted from the own ship (e, f). Those BC particles with Feret diameters greater than 2 μm during stop were fractal aggerates which unlikely survived during long-range transport due to deposition. In addition, heavily coated internal BC particles were found during stop due to the mixing between ship pollution and the marine air (Fig. S5).~~ The bottom panels of Fig. 6 ~~Fig. 5~~ (a-f) show the corresponding images obtained by boxing counting in fractal analysis with the resultant D_f, Feret diameter (D), Lacunarity (L), and sampling number underneath for each TEM sample image. Figure 7 ~~Figure 6~~ shows D_f and L as a function of D for some representative BC particles during both navigation and stop. The BC particles showed narrower Feret diameters (229–2557 nm) during navigation than those (78-2926 nm) of BC from the own ship during stop. ~~These particles were exposed to electron beam and volatile coatings were removed so that the morphology of bare BC was clearly shown regardless of the mixing state of the original BC.~~ The D_f values during navigation were in a range of 1.28 ~~1.50~~–1.77 with a median of 1.65 ~~1.61~~, while the D_f values during stop were 1.43–1.76 ~~1.48–1.75~~ with a median of 1.66 ~~61~~, indicating no significant differences of D_f ~~(<1%)~~ for the exposed BC particles during navigation and stop. Note that the particles in Figure 7 include pure BC and BC without thick coatings. These particles were exposed to the electron beam and volatile coatings were removed so that the morphology of BC was clearly shown regardless of the mixing state of the original BC particles (Figure S7). Most BC particles were below 1 μm in Feret diameter during navigation (Figure 7), while their sizes cover a wide range below 3 μm during stop, implying that the aged BC particles become smaller after long-range transport. Despite only a total of 134 BC data points shown in Figure 7, the results are still statistically meaningful due to the wide range of BC sizes covered in our analysis. Note that the size change of a BC particle cannot be determined because the original size of the particle is unknown before the removal of the coatings. ~~Figure 6 also shows that most of the BC particles during navigation were below 1 μm in Feret diameter, implying that smaller BC particles were more susceptible to be coated and aged during transport.~~ Comparatively, the lacunarities during navigation (0.32 ~~34~~–0.82 ~~90~~, median: 0.53) and stop (0.35 ~~34~~–0.92 ~~77~~, median: 0.59) were different, with the former being smaller than the latter, indicating that the lacunarity tended to become smaller (~10%) after coating or aging of

409 the BC particles.

410 Tar balls were frequently observed during the campaign with an estimated sample fraction of about 11.8%. Fractal-like tar

411 ball aggregates were usually found in wildfire smokes (Girotto et al., 2018); however, in this study, spherical tar ball particles

412 were observed in the marine atmosphere and were mixed with sea salt (Fig. 8a and d for TEM image and EDS spectrum,

413 respectively), organic carbon and sulfate (Fig. 8b and e) from the samples collected on May 27 during navigation. In contrast,

414 the particles collected on June 01 were found to be amorphous carbon agglomerates (Fig. 8c and f) which were referred to OC.

415 ~~Tar balls were frequently observed during the campaign. The spherical tar ball particles in the marine atmosphere were mixed~~

416 ~~with sea salt (Fig. 7a and d for TEM image and EDS spectrum, respectively), organic carbon and sulfate (Fig. 6b and e) from~~

417 ~~the samples collected on May 27 during navigation. In contrast, the particles collected on June 01 were found to be amorphous~~

418 ~~carbon agglomerates which were mixed with sulfate (Fig. 6c and f).~~ During these days, the wind directions were from the

419 southwest, with air masses originating from both the Philippines and Southeast Asia. The shape difference between the tar ball

420 spheres and the amorphous carbon agglomerates may be related to the type of biomass burning or the origin of the ship

421 engines.~~The difference between tar ball spheres and amorphous carbon agglomerates may be related to biomass burning type~~

422 ~~or source origin.~~ Similar particle morphologies were found in other studies on brown carbon during aircraft measurements

423 over the Yellow Sea in 2001 (Zhu et al., 2013). Tar balls mixed with BC during stop were also observed (Fig. S10~~Fig. S6~~),

424 with geometrical diameters of 160–420 nm, much larger than nano-soot spheres (40−50 nm) (Fig. S11~~Fig. S7~~). In comparison,

425 the laboratory-generated tar balls were measured to have AAE values of 2.7–3.4, with an average of 2.9 at 467–652 nm (Hoffer

426 et al., 2016).

427 **3.3 Light absorption of carbonaceous aerosols**~~**Air mass trajectories and mass concentrations of carbonaceous aerosols**~~

428 ~~Figure 8 shows the time series of fire spots distribution and the 72 h backward trajectories at three AGLs (100, 500 and 1000~~

429 ~~m) over the SCS during the campaign. Only several backward trajectories are shown to avoid massive overlapping. Several~~

430 ~~fire spots located in the sea were attributed to oil or natural gas drilling processes which generate thermal energy, combustion,~~

431 ~~and exhaust. Such processes included the prevalent hydrocarbon exploration and production activities in this region. A~~

432 ~~comprehensive cartographic representation of these endeavors within the SCS can be accessed via the online platforms~~

445 The BC concentrations measured by the Magee AE33 aethalometer agree excellently with the optical EC concentrations

446 obtained from the Sunset OC/EC analyzer, as evidenced by a linear regression coefficient of 0.97. The BC measurements

447 obtained from the AE33 instrument do not agree with the OC, EC values, yet their overall trends exhibit consistency. However,

448 the BC concentrations were considerably higher than the thermal EC concentrations, exhibiting linear regression coefficients

449 of 1.66 and 1.55, respectively. These findings, presented in Fig. S12 of Section 8 in the SI Fig. S8 of Section 5 in the SI, are in

450 line with previous research conducted by Brown et al. (2019). The OC/EC ratios can be used as an indicator for the source

451 origins of the air masses. Figure 9 shows the distribution of the OC/EC ratios and the corresponding EC concentrations. Figure

452 9 shows tThe median OC/EC ratios (are 8.14, 5.20, 6.35 and 2.63) for the classified periods (BMP, TMP, AMP, and SPP,

453 respectively). Notably, EC median mass concentrations (0.24, 0.25 and 0.17 $\mu g\ m^{-3}$) for the marine air masses during BMP

454 (0.013−0.69 $\mu g\ m^{-3}$), TMP (0.015−0.60 $\mu g\ m^{-3}$), AMP (0.014−0.74 $\mu g\ m^{-3}$) were lower than the median concentration (1.70 μg

455 m^{-3}) during SPP. Compared with Figure 9d, the scattered higher OC/EC ratios in Figure 9a/b/c are caused by the very low EC

456 concentrations. The presence of extremely low EC concentrations, often falling below or near the detection limit, can introduce

457 discrepancies in the calculation of the OC/EC split, ultimately resulting in inaccurate EC concentrations (Bauer et al., 2009).

458   In addition, this study revealed a significant variation in EC concentrations during SPP, ranging from 0.15 to 22.8 μg m^{-3}.

459   Previous studies showed that OC/EC ratio could be characterized by various sources, ranging from 1.37–1.71 for residential

460   cookstoves, 1.63–2.23 for rural emissions, 1.05–1.24 for diesel exhaust, and 0.80–1.12 for urban environments (Khan et al.,

461   2012). A low OC/EC ratio (<3) corresponded to the predominant contribution of the primary OC in submicron particles

462   reported in a previous study in the Southern Indian Ocean, Northern Indian Ocean and Bay of Bengal (Neusüß, 2002). Here,

463   the median OC/EC ratio of 2.63 during SPP is much higher than the characteristic values of diesel combustion, most likely

464   because the sample air during SPP is composed of marine air and the own ship exhaust. Our results are consistent with a recent

465   study which showed that the diesel combustion from ships accounted for 15% of BrC in the total light absorption at a coastal

466   site in Shanghai during June–July, 2021 (Kang et al., 2022). In contrast, the OC/EC ratios during other periods (i.e., BMP,

467   TMP and AMP) were even much higher (5.20–8.13), indicating that the aerosols were highly aged during the long-range

468   transport of biomass burning aerosols. This is also consistent with our recent study in the SCS which showed that during

469   monsoon periods in the summer of 2019. The biomass burning organic aerosols became aged through atmospheric processes

470   during transport (Sun et al., 2023).

471   ~~3.5 Light absorption of carbonaceous aerosols~~

472   The long-range biomass burning transport affects the air mass in the SCS. Figure 10 illustrates the wavelength-dependent

473   mass concentration measured by the AE33 aethalometer during the campaign, showing (a) an example of a ship plume, and

474   (b, c) two significant biomass burning events during BMP (BB-1: 6:00−7:00 on May 15 and 15:00−22:00 on May 16) and

475   during TMP (BB-2: 15:00 on May 30−00:00 on May 31). The ship plumes, predominantly emitted from fossil fuel combustion,

476   showed similar absorption at all seven wavelengths. In contrast, significant absorption at low wavelengths was detected during

477   the biomass burning events, a phenomenon also observed in other field measurements in urban cities and towns where air

478   masses were susceptible to biomass burning (Zhang et al., 2017). A comparison of the two methods for AAE calculation is

479   presented in the SI (Section 4, Fig. S4~~Section 6, Fig. S9~~). The fitting results demonstrate that the AAE calculated for all

480   wavelengths was lower than the AAE calculated for only 470 and 950 nm wavelengths. The fitting slope is 0.78, and the

481   determination coefficient (R^2) is 0.98, indicating a strong correlation between the two methods.

482   Figure 11 shows the hourly averaged AAE derived from all wavelengths as a function of the BC concentrations by AE33

483   aethalometer with the median (range) AAE values of 1.14 (0.57−1.48), 1.02 (0.51−1.36), 1.08 (0.54−1.42), and 1.06 (0.65−

484   1.37), respectively, for the classified periods (BMP, TMP, AMP, and SPP), and the corresponding BC median (range) mass

485   concentrations of 0.28 (0.033−1.17), 0.14 (0.042−2.86), 0.17 (0.055−1.08), and 3.01 (0.21−36.5) μg m^{-3}, respectively. Like

486   EC, ship pollution led to emissions of high BC concentrations, reaching as high as 36.5 μg m^{-3}. The median BC concentrations

487   decreased significantly during TMP and AMP, likely due to the increase of the RH which further increased the scavenging of

488   the BC particles during navigation as reported previously (Girach et al., 2014). Note that the biomass burning events were

489   excluded from the above calculations and are further discussed below.

490   During the biomass burning events, the correlations of AAE with AE33 BC and Delta-C concentrations are respectively

491   shown in Figs. 11 and 12, characterized by very high median AAE values (1.85 and 1.86, respectively for BB-1 and BB-2) and

492   BC concentrations (1.93 and 1.67 μg m^{-3}). The BC mass concentration ranged from 1.45 to 3.62 μg m-3 during biomass burning

493   events based on light absorption at wavelength of 880 nm. The mass concentration in Figure 10 corresponds to BC mass

494   concentration obtained at each wavelength. We have emphasized that BC mass concentration in this study is equivalent BC at

495   individual wavelength. Notably, efficient light absorption of BrC in the range at 370–660 nm was observed during the biomass

496   burning events, while no significant wavelength-dependent BC concentrations were found during the own ship pollution (Fig.

497   10a). The AAE values below 1 in Figure 11 are not noises, in some cases due to aerosols from fossil fuel (Ezani et al., 2021)

498   and in other cases, they can be even lower than 0.5 when paired with wavelengths of 470 and 660 nm (Laing et al.,

499   2020).Notably, high BC (1.45–3.62 μg m^{-3}) mass concentrations at 370–660 nm were observed during the biomass burning

500   events due to more efficient light absorption of BrC in the range than at higher wavelengths, while no significant wavelength-

501   dependent BC concentrations were found during ship pollution (Fig. 10a). The higher AAE values imply much stronger

502   absorption of non-BC light-absorbing particles (BrC) at shorter (UV-vis) wavelengths, which mainly originated from the

503   biomass burning emissions (Ponczek et al., 2022). Moreover, the median OC/EC ratios were 5.03 and 5.29 respectively for the

504   two biomass burning events, even much higher than those for SPP (Fig. 9). The 72-h backward trajectories also showed that

505   the BB-1 air masses mainly originated from the Philippines while the BB-2 air masses were from the mainland Vietnam, both

506   with high densities of fire spots (Fig. 4Fig. 8). The AAE values were also highly correlated with the Delta-C values with a

507 determination coefficient (R^2) of 0.92 (Fig. 12), further demonstrating a significant contribution of BrC to the AAE

508 enhancement. In addition, we further correlated the observed high AAE values with the Delta-C values for the two biomass

509 burning events and confirmed that these high AAE values (1.45–3.62) were indeed attributed to biomass burning rather than

510 ship emitted tar balls which covered an AAE range of 2.7–3.7 at 405 and 781 nm wavelengths in a previous wood burning

511 study (Chylek et al., 2019).

512   Our study found that the AAE values from all wavelengths for the marine atmosphere and ship pollution were 1.02–1.14

513 and 1.06, respectively, except for a higher AAE value (1.93) during the two biomass burning events. The AAE values for ship

514 pollution are dependent on the fuel types and loading conditions (Laskin et al., 2015). For example, heavy fuel oil operated at

515 high loads can result in AAE values (at 470/950 nm, and hereafter unless specified) of 2.0, while the intermediate fuel oil has

516 an AAE value of 1.3 at high loads (Helin et al., 2021). In addition, the presence of tar balls may contribute to the enhancement

517 of BrC absorption as mentioned in Section 3.2, as tar balls from ship emission have higher AAE values (2.5–6 depending on

518 the wavelengths) (Corbin et al., 2019). The occurrence of tar balls in this study was about 12% in the analyzed single samples.

519 These tar balls were likely aged during long-range transport from biomass burning and hence affected the light absorption of

520 BrC in the SCS.

521 **~~3.6~~3.4 BC sources from fossil fuel vs biomass burning**

522 The source origins of BC particles can be investigated using the AAE model. In the model, we employed respectively the

523 characteristic AAE values of 1 and 2 for FF and BB to calculate their corresponding BC concentrations, namely BC(FF) and

524 BC(BB). Figure 13 shows the time series of BC(FF) and BC(BB) for different classified periods. The BC(FF) and BC(BB)

525 values were much higher before the monsoon than during/after the monsoon, except for the periods during BB-1 and BB-2

526 with significantly high BC(FF) and BC(BB) values (peaks > 1 µg m^{-3}), while high BC(FF) values were seen during SPP. Table

527 2 summarizes the average concentrations and the ranges of BC(FF) and BC(BB), along with their corresponding fractions. In

528 general, both the average BC(FF) and BC(BB) values were low during BMP, TMP, and AMP, compared to those during the

529 biomass burning events and SPP. BC(FF) contributed over 80% of ship pollution during SPP, whilst the BC(BB) could

530 contribute to more than 40% of the total black carbon during the two BB events. We hence conclude that fossil fuel combustion

22

531 is the major contributor to the light absorption of BC except during the seasonal biomass burning events and biomass burning

532 can have a profound contribution to the BC light absorption in the SCS.

533   Active biomass burning pollution during January–May in Southeast Asia occurs routinely because of crop residue and sugar

534 cane burning. A previous study showed that during dry and wet seasons, the annual contribution of BC(BB) was 11% and 30%

535 respectively in the Peninsular India (Soyam, 2021) based on the two-component AAE model (Drinovec et al., 2015; Yus-Díez

536 et al., 2021). Table 3 summarizes the BC concentrations, AAE values, and the corresponding fraction of biomass burning (or

537 fossil fuel) in previous and present studies for the marine atmosphere conducted at coastal sites or ship-based cruise

538 measurements using the AE series instrument. The BC(FF) and BC(BB) fractions of 58% and 42% were obtained respectively

539 during the two BB events, while they accounted for 78–83% and 18–22% during other periods, similar to those found at the

540 coastal site in Central Adriatic (79% and 21%), and significantly different from those reported at a coastal site in the East China

541 Sea (Yu et al., 2018). However, observation data are still lacking on the contribution of BC from fossil fuel vs biomass burning

542 in the sea regions which warrants more future studies during different seasons.

543 **3.7 3.5 Limitation of this study**

544 This cruise campaign for carbonaceous aerosols has several limitations which might need to be aware of due to the time and

545 area coverage constraints. The presence of other light-absorption aerosol components, polluted dusts, oil and gas drilling

546 emissions, as well as fishery policy may contribute to the uncertainties in the AAE model used for the BC source

547 apportionment in this study. Firstly, the composition of aerosols and refractive index may strongly affect the AAE calculation.

548 The source apportionment of BC for biomass burning and foil fuel is based on the AAE two-component model which only

549 considered BC(BB) and BC(FF) as the light absorption materials. An AAE range of 0.9–1.4 is used for pure BC from foil fuel

550 emissions, while it is 1.68–2.2 for biomass burning as mentioned earlier. The current AAE two-component model does not

551 include other potential light-absorbing materials, such as mineral dust and biological particles (Pileci et al., 2021). Interestingly,

552 two types of possible biological particles were observed during the campaign (Fig. S13Fig. S10, in the SI, section 79). A similar

553 type of biological particles was observed and identified as brocosomes in another campaign near the East China Sea (Fu et al.,

554 2012). However, more future studies are needed to identify the types and species of biological particles and to evaluate their

23

555 contributions to the light-absorption.

556 Secondly, based on the Cloud-Aerosol Lidar & Infrared Satellite Observation (CALIPSO) data on May 15 and June 07 when

557 the orbit just passed over the SCS region and the Southeast Asia (Fig. S14 and S15~~Fig. S11 and S12~~, in the SI, section ~~8~~10),

558 we found the presence of polluted dust in the vertical profile over the Philippines, Indonesia, Thailand and Malaysia. Long-

559 range transport of dust may affect our measured AAE data. Thirdly, oil and natural gas drilling (Liu and Li, 2021) is active in

560 the SCS region and the distribution map is available online (https://www.oilmap.xyz/). These activities potentially contribute

561 to the BC emissions (Cordes et al., 2016), and these BC are similar to those of continental emitted BC from incomplete burning

562 of oil or natural gas.

563 Lastly, Chinese fishery policy enacts fishing prohibition for about three and a half months every year in the SCS during

564 summer which corresponds to May 01–Aug 16 in the year of 2021 in 12°N within our campaign region. Therefore, the cruise

565 measurements mainly captured ship emissions from the commercial ships in the SCS whose routes are available online

566 (https://www.marinetraffic.com/en/ais/home/centerx:116.6/centery:20.5/zoom:4). The average BC mass concentrations (~0.2

567 µg m^{-3} for BC(FF) and 0.05–0.08 µg m^{-3} for BC(BB) are only limited to data of about a month and the coverage area. Hence,

568 more future measurements covering more seasons and wider areas are needed to better understand the morphology and optical

569 properties of the carbonaceous aerosols in the SCS.

570 **5. Conclusions**

571 As important components of carbonaceous aerosols, BC and BrC in the marine atmosphere may exert significantly positive

572 climatic radiative forcing through light absorption on the regional and global scales. However, quantification of their absorption

573 potential is tremendously challenging due to little knowledge on the microphysical properties, such as morphology, particle

574 size, and mixing state of BC or BrC in the marine region such as SCS. This ship-based study is intended to investigate the

575 morphological and optical properties of the BC particles in the SCS during summer using a combined online aethalometer,

576 semi-online OC/EC analyzer, and offline TEM/EDS analyses. The results showed that the lognormal fitted Feret diameter

577 distribution of the single particles peaks at 325 nm when the ship stopped, while it peaks at 307 nm when the ship navigated.

578 This minor difference in the size distribution could be attributed to the distinguishable air mass origins of the own ship

579 emissions for the former and the mixed other ship emissions and long-range transport for the latter. Furthermore, the Feret

580 diameters of the single particles spread much more narrowly during navigation (229-2557~~298 1980~~ nm) than those of the

581 freshly emitted particles during stop (78-2926~~304 2982~~ nm). In addition, the two types of single particles have ~~similar~~ same

582 median fractal dimension values (~~1.65 vs 1.66~~1.61) but different lacunarity values (0.53 vs 0.59), indicating their different

583 aging degrees. The aged BC particles are present in various mixing states (core-shell, embedded, external) with other aerosol

584 components after long-range transport. Interestingly, a fraction of single particles ~~was~~ were identified as tar balls with

585 geometrical diameters of 160–420 nm which were primarily mixed with sea salt, organics, BC, and sulfate, and those tar balls

586 were found to originate from either ship emissions or long-range transport of biomass burning.

587   Since the marine atmosphere is mainly subject to the influence of biomass burning and fossil fuel combustion, a two-

588 component (BB and FF) AAE model was employed to evaluate the source contributions to the light absorption of the BC

589 particles. The modelling results indicated that BB and FF contributed respectively to 18–22% and 78–82% of all the BC light

590 absorption except for a substantial percentage of 42% for BB (hence 58% for FF) during the two observed significant biomass

591 burning events. The results from trajectory calculations showed that biomass burning was predominantly from the Philippines

592 and South East Asia before and after the summer monsoon during the cruise campaign. However, this highly simplified two-

593 component AAE model may have substantial uncertainties ~~on~~ in the evaluation of the source contributions when other sources

594 of BC particles were present and those included dust, biological materials, oil and gas drilling emissions during the

595 measurements. Nevertheless, this study demonstrates that emissions from ~~the~~ commercial ships and biomass burning from

596 Southeast Asia contribute to the enhanced light absorption of the BC particles in the SCS, especially during the crop harvest

597 seasons before monsoon, and the aged BC particles became more aggerated after long-range transport of air masses containing

598 biomass burning emissions.

Author contributions

600 JZ, CZS, and SZZ planned the cruise campaign. CZS, YYZ, BLL, MG, and XS performed the measurements. CZS performed

601 the data analysis and wrote the original draft. CZS and DXC performed funding acquisition. JZ and SZZ performed funding

602 acquisition and supervision. All authors reviewed and edited the manuscript.

Declaration of competing interest

The authors declare no conflict of interest.

Data availability

Data for figures and tables, along with raw data from online measurements and offline analyses of this study are available from JZ via zhaojun23@mail.sysu.edu.cn upon request. The supplementary data are available online at xxx.

Acknowledgements

References

Adachi, K., Zaizen, Y., Kajino, M., and Igarashi, Y.: Mixing state of regionally transported soot particles and the coating effect on their size and shape at a mountain site in Japan, J. Geophys. Res. Atmos., 119, 5386-5396, https://doi.org/10.1002/2013jd020880, 2014.

Adachi, K., Sedlacek, A. J., III, Kleinman, L., Springston, S. R., Wang, J., Chand, D., Hubbe, J. M., Shilling, J. E., Onasch, T. B., Kinase, T., Sakata, K., Takahashi, Y., and Buseck, P. R.: Spherical tarball particles form through rapid chemical and physical changes of organic matter in biomass-burning smoke, Proc. Natl. Acad. Sci. U.S.A., 116, 19336-19341, https://doi.org/10.1073/pnas.1900129116, 2019.

Alroe, J., Cravigan, L. T., Miljevic, B., Johnson, G. R., Selleck, P., Humphries, R. S., Keywood, M. D., Chambers, S. D., Williams, A. G., and Ristovski, Z. D.: Marine productivity and synoptic meteorology drive summer-time variability in

627   Southern Ocean aerosols, Atmos. Chem. Phys. Discuss., https://doi.org/10.5194/acp-2019-1081, 2019.

628   Andreae, M. O. and Gelencsér, A.: Black carbon or brown carbon? The nature of light-absorbing carbonaceous aerosols, Atmos.
629   Chem. Phys., 6, 3131-3148, https://doi.org/10.5194/acp-6-3131-2006, 2006.

630   Ausmeel, S., Eriksson, A., Ahlberg, E., Sporre, M. K., Spanne, M., and Kristensson, A.: Ship plumes in the Baltic Sea sulfur
631   emission control area: Chemical characterization and contribution to coastal aerosol concentrations, Atmos. Chem. Phys.,
632   20, 9135-9151, https://doi.org/10.5194/acp-20-9135-2020, 2020.

633   Bao, M., Zhang, Y., Cao, F., Lin, Y., Wang, Y., Liu, X., Zhang, W., Fan, M. Y., Xie, F., Cary, R. A., Dixon, J., and Zhou, L.:
634   Highly time-resolved characterization of carbonaceous aerosols using a two-wavelength Sunset thermal–optical carbon
635   analyzer, Atmos. Meas. Tech., 14, 4053-4068, https://doi.org/10.5194/amt-14-4053-2021, 2021.

636   Bauer, J. J., Yu, X.-Y., Cary, R., Laulainen, N., and Berkowitz, C.: Characterization of the Sunset semi-continuous carbon
637   aerosol analyzer, J. Air Waste Manag. Assoc., 59, 826-833, https://doi.org/10.3155/1047-3289.59.7.826, 2012.

638   Bencs, L., Horemans, B., Buczyńska, A. J., Deutsch, F., Degraeuwe, B., Van Poppel, M., and Van Grieken, R.: Seasonality of
639   ship emission related atmospheric pollution over coastal and open waters of the North Sea, Atmos. Environ.: X., 7,
640   https://doi.org/10.1016/j.aeaoa.2020.100077, 2020.

641   Blanco-Donado, E. P.: Source identification and global implications of black carbon, Geosci. Front.,
642   https://doi.org/10.1016/j.gsf.2021.101149, 2022.

643   Bond, T. C., Doherty, S. J., Fahey, D. W., Forster, P. M., Berntsen, T., DeAngelo, B. J., Flanner, M. G., Ghan, S., Kärcher, B.,
644   Koch, D., Kinne, S., Kondo, Y., Quinn, P. K., Sarofim, M. C., Schultz, M. G., Schulz, M., Venkataraman, C., Zhang, H.,
645   Zhang, S., Bellouin, N., Guttikunda, S. K., Hopke, P. K., Jacobson, M. Z., Kaiser, J. W., Klimont, Z., Lohmann, U., Schwarz,
646   J. P., Shindell, D., Storelvmo, T., Warren, S. G., and Zender, C. S.: Bounding the role of black carbon in the climate system:
647   A scientific assessment, J. Geophys. Res. Atmos., 118, 5380-5552, https://doi.org/10.1002/jgrd.50171, 2013.

648   Brown, S., Minor, H., O'Brien, T., Hameed, Y., Feenstra, B., Kuebler, D., Wetherell, W., Day, R., Tun, R., Landis, E., and Rice,
649   J.: Review of Sunset OC/EC instrument measurements during the EPA's Sunset carbon evaluation project, Atmosphere
650   (Basel), 10, 287, https://doi.org/10.3390/atmos10050287, 2019.

651   Budhavant, K., Andersson, A., Holmstrand, H., Bikkina, P., Bikkina, S., Satheesh, S. K., and Gustafsson, Ö.: Enhanced light-
652   absorption of black carbon in rainwater compared with aerosols over the Northern Indian Ocean, J. Geophys. Res. Atmos.,
653   125, https://doi.org/10.1029/2019jd031246, 2020.

654   Cai, M., Liang, B., Sun, Q., Zhou, S., Chen, X., Yuan, B., Shao, M., Tan, H., and Zhao, J.: Effects of continental emissions on
655   cloud condensation nuclei (CCN) activity in the northern South China Sea during summertime 2018, Atmos. Chem. Phys.,
656   20, 9153-9167, https://doi.org/10.5194/acp-20-9153-2020, 2020.

657   Cappa, C. D., Onasch, T. B., Massoli, P., Worsnop, D. R., Bates, T. S., Cross, E. S., Davidovits, P., Hakala, J., Hayden, K. L.,
658   Jobson, B. T., Kolesar, K. R., Lack, D. A., Lerner, B. M., Li, S.-M., Mellon, D., Nuaaman, I., Olfert, J. S., Petäjä, T., Quinn,
659   P. K., Song, C., Subramanian, R., Williams, E. J., and Zaveri, R. A.: Radiative absorption enhancements due to the mixing
660   state of atmospheric black carbon, Science, 337, 1078, https://doi.org/10.1126/science.1223447, 2012.

661   Chakrabarty, R. K., Moosmüller, H., Garro, M. A., Arnott, W. P., Walker, J., Susott, R. A., Babbitt, R. E., Wold, C. E., Lincoln,
662   E. N., and Hao, W. M.: Emissions from the laboratory combustion of wildland fuels: Particle morphology and size, J.
663   Geophys. Res., 111, https://doi.org/10.1029/2005jd006659, 2006.

Chaubey, J. P., Moorthy, K. K., Babu, S. S., and Gogoi, M. M.: Spatio-temporal variations in aerosol properties over the oceanic regions between coastal India and Antarctica, J. Atmos. Sol. Terr. Phys., 104, 18-28, https://doi.org/10.1016/j.jastp.2013.08.004, 2013.

Chen, D., Cui, H., Zhao, Y., Yin, L., Lu, Y., and Wang, Q.: A two-year study of carbonaceous aerosols in ambient PM2.5 at a regional background site for western Yangtze River Delta, China, Atmos. Res., 183, 351-361, https://doi.org/https://doi.org/10.1016/j.atmosres.2016.09.004, 2017.

Chen, X., Ye, C., Wang, Y., Wu, Z., Zhu, T., Zhang, F., Ding, X., Shi, Z., Zheng, Z., and Li, W.: Quantifying evolution of soot mixing state from transboundary transport of biomass burning emissions, iScience, 26, 108125, 10.1016/j.isci.2023.108125, 2023.

Cheng, Z., Sharma, N., Tseng, K. P., Kovarik, L., and China, S.: Direct observation and assessment of phase states of ambient and lab-generated sub-micron particles upon humidification, RSC Adv, 11, 15264-15272, 10.1039/d1ra02530a, 2021.

China, S., Mazzoleni, C., Gorkowski, K., Aiken, A. C., and Dubey, M. K.: Morphology and mixing state of individual freshly emitted wildfire carbonaceous particles, Nat. Commun., 4, 2122, https://doi.org/10.1038/ncomms3122, 2013.

Chylek, P., Lee, J. E., Romonosky, D. E., Gallo, F., Lou, S., Shrivastava, M., Carrico, C. M., Aiken, A. C., and Dubey, M. K.: Mie scattering captures observed optical properties of ambient biomass burning plumes assuming uniform black, brown, and organic carbon mixtures, J. Geophys. Res. Atmos., 124, 11406-11427, https://doi.org/10.1029/2019jd031224, 2019.

Corbin, J. C., Czech, H., Massabò, D., de Mongeot, F. B., Jakobi, G., Liu, F., Lobo, P., Mennucci, C., Mensah, A. A., Orasche, J., Pieber, S. M., Prévôt, A. S. H., Stengel, B., Tay, L. L., Zanatta, M., Zimmermann, R., El Haddad, I., and Gysel, M.: Infrared-absorbing carbonaceous tar can dominate light absorption by marine-engine exhaust, npj Clim. Atmos. Sci., 2, https://doi.org/10.1038/s41612-019-0069-5, 2019.

Cordes, E. E., Jones, D. O. B., Schlacher, T. A., Amon, D. J., Bernardino, A. F., Brooke, S., Carney, R., DeLeo, D. M., Dunlop, K. M., Escobar-Briones, E. G., Gates, A. R., Génio, L., Gobin, J., Henry, L.-A., Herrera, S., Hoyt, S., Joye, M., Kark, S., Mestre, N. C., Metaxas, A., Pfeifer, S., Sink, K., Sweetman, A. K., and Witte, U.: Environmental impacts of the deep-water oil and gas industry: A review to guide management strategies, Front. Environ. Sci., 4, https://doi.org/10.3389/fenvs.2016.00058, 2016.

Dong, Z., Kang, S., Qin, D., Shao, Y., Ulbrich, S., and Qin, X.: Variability in individual particle structure and mixing states between the glacier–snowpack and atmosphere in the northeastern Tibetan Plateau, The Cryosphere, 12, 3877-3890, 10.5194/tc-12-3877-2018, 2018.

Drinovec, L., Močnik, G., Zotter, P., Prévôt, A. S. H., Ruckstuhl, C., Coz, E., Rupakheti, M., Sciare, J., Müller, T., Wiedensohler, A., and Hansen, A. D. A.: The "dual-spot" Aethalometer: An improved measurement of aerosol black carbon with real-time loading compensation, Atmos. Meas. Tech., 8, 1965-1979, https://doi.org/10.5194/amt-8-1965-2015, 2015.

Duarte, R. M. B. O., Gomes, J. F. P., Querol, X., Cattaneo, A., Bergmans, B., Saraga, D., Maggos, T., Di Gilio, A., Rovelli, S., and Villanueva, F.: Advanced instrumental approaches for chemical characterization of indoor particulate matter, Appl. Spectrosc. Rev., 57, 705-745, https://doi.org/10.1080/05704928.2021.2018596, 2021.

Ezani, E., Dhandapani, S., Heal, M. R., Praveena, S. M., Khan, M. F., and Ramly, Z. T. A.: Characteristics and source apportionment of black carbon (BC) in a suburban area of Klang Valley, Malaysia, Atmosphere, 12, https://doi.org/10.3390/atmos12060784, 2021.

Feng, X., Wang, J., Teng, S., Xu, X., Zhu, B., Wang, J., Zhu, X., Yurkin, M. A., and Liu, C.: Can light absorption of black carbon still be enhanced by mixing with absorbing materials?, Atmos. Environ., 253, 118358, https://doi.org/10.1016/j.atmosenv.2021.118358, 2021.

Fossum, K. N., Ovadnevaite, J., Liu, D., Flynn, M., O'Dowd, C., and Ceburnis, D.: Background levels of black carbon over remote marine locations, Atmos. Res., 271, https://doi.org/10.1016/j.atmosres.2022.106119, 2022.

Fu, H., Zhang, M., Li, W., Chen, J., Wang, L., Quan, X., and Wang, W.: Morphology, composition and mixing state of individual carbonaceous aerosol in urban Shanghai, Atmos. Chem. Phys., 12, 693-707, https://doi.org/10.5194/acp-12-693-2012, 2012.

Geron, C.: Carbonaceous aerosol over a Pinus taeda forest in Central North Carolina, USA, Atmos. Environ., 43, 959-969, https://doi.org/10.1016/j.atmosenv.2008.10.053, 2009.

Giglio, L., Schroeder, W., Hall, J. V., and Justice, C. O.: MODIS collection 6 active fire product user's guide revision C, University of Maryland. National Oceanic and Atmospheric Administration, 63 pp., 2020.

Girach, I. A., Nair, V. S., Babu, S. S., and Nair, P. R.: Black carbon and carbon monoxide over Bay of Bengal during W_ICARB: Source characteristics, Atmos. Environ., 94, 508-517, https://doi.org/10.1016/j.atmosenv.2014.05.054, 2014.

Girotto, G., China, S., Bhandari, J., Gorkowski, K., Scarnato, B. V., Capek, T., Marinoni, A., Veghte, D. P., Kulkarni, G., Aiken, A. C., Dubey, M., and Mazzoleni, C.: Fractal-like tar ball aggregates from wildfire smoke, Environ. Sci. Technol. Lett., 5, 360-365, 10.1021/acs.estlett.8b00229, 2018. Hand, J. L., Malm, W. C., Laskin, A., Day, D., Lee, T., Wang, C., Carrico, C., Carrillo, J., Cowin, J. P., Collett, J., and Iedema, M. J.: Optical, physical, and chemical properties of tar balls observed during the Yosemite Aerosol Characterization Study, J. Geophys. Res., 110, https://doi.org/10.1029/2004jd005728, 2005.

Harrison, R. M.: Airborne particulate matter, Philos. Trans. R. Soc. A, 378, 20190319, https://doi.org/10.1098/rsta.2019.0319, 2020.

Helin, A., Virkkula, A., Backman, J., Pirjola, L., Sippula, O., Aakko-Saksa, P., Väätäinen, S., Mylläri, F., Järvinen, A., Bloss, M., Aurela, M., Jakobi, G., Karjalainen, P., Zimmermann, R., Jokiniemi, J., Saarikoski, S., Tissari, J., Rönkkö, T., Niemi, J. V., and Timonen, H.: Variation of absorption Ångström exponent in aerosols from different emission sources, J. Geophys. Res. Atmos., 126, https://doi.org/10.1029/2020jd034094, 2021.

Hoffer, A., Tóth, A., Nyirő-Kósa, I., Pósfai, M., and Gelencsér, A.: Light absorption properties of laboratory-generated tar ball particles, Atmos. Chem. Phys., 16, 239-246, https://doi.org/10.5194/acp-16-239-2016, 2016.

Jung, J., Kim, Y. J., Lee, K. Y., Kawamura, K., Hu, M., and Kondo, Y.: The effects of accumulated refractory particles and the peak inert mode temperature on semi-continuous organic carbon and elemental carbon measurements during the CAREBeijing 2006 campaign, Atmos. Environ., 45, 7192-7200, https://doi.org/10.1016/j.atmosenv.2011.09.003, 2011.

Kang, H., Shang, X., Abdumutallip, M., Chen, Y., Li, L., Wang, X., Li, C., Ouyang, H., Tang, X., Wang, L., Rudich, Y., and Chen, J.: Accurate observation of black and brown carbon in atmospheric fine particles via a versatile aerosol concentration enrichment system (VACES), Sci. Total Environ., 837, 155817, https://doi.org/10.1016/j.scitotenv.2022.155817, 2022.

Karanasiou, A., Panteliadis, P., Perez, N., Minguillon, M. C., Pandolfi, M., Titos, G., Viana, M., Moreno, T., Querol, X., and Alastuey, A.: Evaluation of the Semi-Continuous OCEC analyzer performance with the EUSAAR2 protocol, Sci. Total Environ., 747, 141266, https://doi.org/10.1016/j.scitotenv.2020.141266, 2020.

Kedia, S., Ramachandran, S., Rajesh, T. A., and Srivastava, R.: Aerosol absorption over Bay of Bengal during winter: Variability and sources, Atmos. Environ., 54, 738-745, https://doi.org/10.1016/j.atmosenv.2011.12.047, 2012.

738 Khan, B., Hays, M. D., Geron, C., and Jetter, J.: Differences in the OC/EC ratios that characterize ambient and source aerosols
739   due to thermal-optical analysis, Aerosol Sci. Technol., 46, 127-137, https://doi.org/10.1080/02786826.2011.609194, 2012.

740 Kompalli, S. K., Babu, S. N. S., Moorthy, K. K., Satheesh, S. K., Gogoi, M. M., Nair, V. S., Jayachandran, V. N., Liu, D.,
741   Flynn, M. J., and Coe, H.: Mixing state of refractory black carbon aerosol in the South Asian outflow over the northern
742   Indian Ocean during winter, Atmos. Chem. Phys., 21, 9173-9199, https://doi.org/10.5194/acp-21-9173-2021, 2021.

743 Kwak, N., Lee, H., Maeng, H., Seo, A., Lee, K., Kim, S., Lee, M., Cha, J. W., Shin, B., and Park, K.: Morphological and
744   chemical classification of fine particles over the Yellow Sea during spring, 2015-2018, Environ. Pollut., 305, 119286,
745   https://doi.org/10.1016/j.envpol.2022.119286, 2022.

746 Lack, D. A. and Cappa, C. D.: Impact of brown and clear carbon on light absorption enhancement, single scatter albedo and
747   absorption wavelength dependence of black carbon, Atmos. Chem. Phys., 10, 4207-4220, 10.5194/acp-10-4207-2010, 2010.

748 Laing, J. R., Jaffe, D. A., and Sedlacek, I. I. I. A. J.: Comparison of Filter-based Absorption Measurements of Biomass Burning
749   Aerosol and Background Aerosol at the Mt. Bachelor Observatory, Aerosol Air Qual. Res., 20, 663-678,
750   10.4209/aaqr.2019.06.0298, 2020.

751 Lappi, M. K. and Ristimaki, J. M.: Evaluation of thermal optical analysis method of elemental carbon for marine fuel exhaust,
752   J. Air Waste Manag. Assoc., 67, 1298-1318, https://doi.org/10.1080/10962247.2017.1335251, 2017.

753 Laskin, A., Laskin, J., and Nizkorodov, S. A.: Chemistry of atmospheric brown carbon, Chem. Rev., 115, 4335-4382,
754   https://doi.org/10.1021/cr5006167, 2015.

755 Li, J., Zhang, Q., Wang, G., Li, J., Wu, C., Liu, L., Wang, J., Jiang, W., Li, L., Ho, K. F., and Cao, J.: Optical properties and
756   molecular compositions of water-soluble and water-insoluble brown carbon (BrC) aerosols in northwest China, Atmos.
757   Chem. Phys., 20, 4889-4904, https://doi.org/10.5194/acp-20-4889-2020, 2020.

758 Liu, J. and Li, X.: Recent advances on natural gas hydrate exploration and development in the South China Sea, Energy Fuels,
759   35, 7528-7552, https://doi.org/10.1021/acs.energyfuels.1c00494, 2021.

760 Liu, L., Zhang, J., Zhang, Y., Wang, Y., Xu, L., Yuan, Q., Liu, D., Sun, Y., Fu, P., Shi, Z., and Li, W.: Persistent residential
761   burning-related primary organic particles during wintertime hazes in North China: insights into their aging and optical
762   changes, Atmos. Chem. Phys., 21, 2251-2265, https://doi.org/10.5194/acp-21-2251-2021, 2021.

763 Liu, X., Zhu, R., Jin, B., Zu, L., Wang, Y., Wei, Y., and Zhang, R.: Emission characteristics and light absorption apportionment
764   of carbonaceous aerosols: A tunnel test conducted in an urban with fully enclosed use of E10 petrol, Environ. Res., 216,
765   https://doi.org/10.1016/j.envres.2022.114701, 2023.

766 Lu, Q., Liu, C., Zhao, D., Zeng, C., Li, J., Lu, C., Wang, J., and Zhu, B.: Atmospheric heating rate due to black carbon aerosols:
767   Uncertainties and impact factors, Atmos. Res., 240, https://doi.org/10.1016/j.atmosres.2020.104891, 2020.

768 Luo, J., Zhang, Y., and Zhang, Q.: Effects of black carbon morphology on brown carbon absorption estimation: From numerical
769   aspects, Geosci. Model Dev., 14, 2113-2126, https://doi.org/10.5194/gmd-14-2113-2021, 2021.

770 Luo, J., Li, Z., Zhang, C., Zhang, Q., Zhang, Y., Zhang, Y., Curci, G., and Chakrabarty, R. K.: Regional impacts of black carbon
771   morphologies on shortwave aerosol–radiation interactions: A comparative study between the US and China, Atmos. Chem.
772   Phys., 22, 7647-7666, https://doi.org/10.5194/acp-22-7647-2022, 2022.

773 Ma, Y., Zhang, X., Xin, J., Zhang, W., Wang, Z., Liu, Q., Wu, F., Wang, L., Lyu, Y., Wang, Q., and Ma, Y.: Mass and number
774   concentration distribution of marine aerosol in the Western Pacific and the influence of continental transport, Environ. Pollut.,

298, 118827, https://doi.org/10.1016/j.envpol.2022.118827, 2022.

Marple, V. A. and Olson, B. A.: Sampling and measurement using inertial, gravitational, centrifugal, and thermal techniques, in: Aerosol measurement: Principles, techniques, and applications, edited by: Kulkarni, P., Baron, P. A., and Willeke, K., John Wiley and Sons, Hoboken, New Jersey, USA, 129-151, https://doi.org/10.1002/9781118001684.ch8, 2011.

Matsui, H., Koike, M., Kondo, Y., Oshima, N., Moteki, N., Kanaya, Y., Takami, A., and Irwin, M.: Seasonal variations of Asian black carbon outflow to the Pacific: Contribution from anthropogenic sources in China and biomass burning sources in Siberia and Southeast Asia, J. Geophys. Res. Atmos., 118, 9948-9967, https://doi.org/10.1002/jgrd.50702, 2013.

Milinković, A., Gregorič, A., Grgičin, V. D., Vidič, S., Penezić, A., Kušan, A. C., Alempijević, S. B., Kasper-Giebl, A., and Frka, S.: Variability of black carbon aerosol concentrations and sources at a Mediterranean coastal region, Atmos. Pollut. Res., 12, https://doi.org/10.1016/j.apr.2021.101221, 2021.

Moschos, V., Gysel-Beer, M., Modini, R. L., Corbin, J. C., Massabò, D., Costa, C., Danelli, S. G., Vlachou, A., Daellenbach, K. R., Szidat, S., Prati, P., Prévôt, A. S. H., Baltensperger, U., and El Haddad, I.: Source-specific light absorption by carbonaceous components in the complex aerosol matrix from yearly filter-based measurements, Atmos. Chem. Phys., 21, 12809-12833, https://doi.org/10.5194/acp-21-12809-2021, 2021.

Neusüß, C.: Carbonaceous aerosol over the Indian Ocean: OC/EC fractions and selected specifications from size-segregated onboard samples, J. Geophys. Res., 107, https://doi.org/10.1029/2001jd000327, 2002.

Pabst, W. and Gregorova, E.: Characterization of particles and particle systems, ICT Prague, 122, 122, 2007.

Pang, Y., Wang, Y., Wang, Z., Zhang, Y., Liu, L., Kong, S., Liu, F., Shi, Z., and Li, W.: Quantifying the fractal dimension and morphology of individual atmospheric soot aggregates, J. Geophys. Res. Atmos., 127, https://doi.org/10.1029/2021jd036055, 2022.

Pankratova, N. V., Belikov, I. B., Belousov, V. A., Kopeikin, V. M., Skorokhod, A. I., Shtabkin, Y. A., Malafeev, G. V., and Flint, M. V.: Concentration and isotopic composition of methane, associated gases, and black carbon over Russian Arctic Seas (shipborne measurements), Oceanology, 60, 593-602, https://doi.org/10.1134/s0001437020050197, 2021.

Park, S., Yu, G.-H., and Lee, S.: Optical absorption characteristics of brown carbon aerosols during the KORUS-AQ campaign at an urban site, Atmos. Res., 203, 16-27, https://doi.org/10.1016/j.atmosres.2017.12.002, 2018.

Peyronel, M. F., Acevedo, N. C., and Marangoni, A. G.: Structural and mechanical properties of fats and their implications for food quality, in: Chemical deterioration and physical instability of food and beverages, edited by: Skibsted, L. H., Risbo, J., and Andersen, M. L., Woodhead Publishing Limited, Abington Hall, Granta Park, Great Abington, Cambridge CB21 6AH, UK, 216-259, https://doi.org/10.1533/9781845699260.2.216, 2010.

Pileci, R. E., Modini, R. L., Bertò, M., Yuan, J., Corbin, J. C., Marinoni, A., Henzing, B., Moerman, M. M., Putaud, J. P., Spindler, G., Wehner, B., Müller, T., Tuch, T., Trentini, A., Zanatta, M., Baltensperger, U., and Gysel-Beer, M.: Comparison of co-located refractory black carbon (rBC) and elemental carbon (EC) mass concentration measurements during field campaigns at several European sites, Atmos. Meas. Tech., 14, 1379-1403, https://doi.org/10.5194/amt-14-1379-2021, 2021.

Pipal, A. S., Rohra, H., Tiwari, R., and Taneja, A.: Particle size distribution, morphometric study and mixing structure of accumulation and ultrafine aerosols emitted from indoor activities in different socioeconomic micro-environment, Atmos. Pollut. Res., 12, 101-111, https://doi.org/10.1016/j.apr.2021.02.015, 2021.

Ponczek, M., Franco, M. A., Carbone, S., Rizzo, L. V., Monteiro dos Santos, D., Morais, F. G., Duarte, A., Barbosa, H. M. J.,

and Artaxo, P.: Linking the chemical composition and optical properties of biomass burning aerosols in Amazonia, Environ. Sci. Atmos., 2, 252-269, https://doi.org/10.1039/d1ea00055a, 2022.

Rabha, S. and Saikia, B. K.: An environmental evaluation of carbonaceous aerosols in PM10 at micro- and nano-scale levels reveals the formation of carbon nanodots, Chemosphere, 244, 125519, https://doi.org/10.1016/j.chemosphere.2019.125519, 2020.

Retama, A., Ramos-Cerón, M., Rivera-Hernández, O., Allen, G., and Velasco, E.: Aerosol optical properties and brown carbon in Mexico City, Environ. Sci. Atmos., 2, 315-334, https://doi.org/10.1039/d2ea00006g, 2022.

Rice, S. B., Chan, C., Brown, S. C., Eschbach, P., Han, L., Ensor, D. S., Stefaniak, A. B., Bonevich, J., Vladar, A. E., Hight Walker, A. R., Zheng, J., Starnes, C., Stromberg, A., Ye, J., and Grulke, E. A.: Particle size distributions by transmission electron microscopy: An interlaboratory comparison case study, Metrologia, 50, 663-678, https://doi.org/10.1088/0026-1394/50/6/663, 2013.

Schmale, J., Baccarini, A., Thurnherr, I., Henning, S., Efraim, A., Regayre, L., Bolas, C., Hartmann, M., Welti, A., Lehtipalo, K., Aemisegger, F., Tatzelt, C., Landwehr, S., Modini, R. L., Tummon, F., Johnson, J. S., Harris, N., Schnaiter, M., Toffoli, A., Derkani, M., Bukowiecki, N., Stratmann, F., Dommen, J., Baltensperger, U., Wernli, H., Rosenfeld, D., Gysel-Beer, M., and Carslaw, K. S.: Overview of the Antarctic Circumnavigation Expedition: Study of Preindustrial-like aerosols and their climate effects (ACE-SPACE), Bull. Am. Meteorol. Soc., 100, 2260-2283, https://doi.org/10.1175/bams-d-18-0187.1, 2019.

Shamjad, P. M., Tripathi, S. N., Aggarwal, S. G., Mishra, S. K., Joshi, M., Khan, A., Sapra, B. K., and Ram, K.: Comparison of experimental and modeled absorption enhancement by black carbon (BC) cored polydisperse aerosols under hygroscopic conditions, Environ. Sci. Technol., 46, 8082-8089, https://doi.org/10.1021/es300295v, 2012.

Shank, L. M., Howell, S., Clarke, A. D., Freitag, S., Brekhovskikh, V., Kapustin, V., McNaughton, C., Campos, T., and Wood, R.: Organic matter and non-refractory aerosol over the remote Southeast Pacific: Oceanic and combustion sources, Atmos. Chem. Phys., 12, 557-576, https://doi.org/10.5194/acp-12-557-2012, 2012.

Sharma, S., Barrie, L. A., Magnusson, E., Brattström, G., Leaitch, W. R., Steffen, A., and Landsberger, S.: A factor and trends analysis of multidecadal lower tropospheric observations of Arctic aerosol composition, black carbon, ozone, and mercury at Alert, Canada, J. Geophys. Res. Atmos., 124, 14133-14161, https://doi.org/10.1029/2019jd030844, 2019.

Song, X., Xie, X., Qiu, B., Cao, H., Xie, S.-P., Chen, Z., and Yu, W.: Air-sea latent heat flux anomalies induced by oceanic submesoscale processes: An observational case study, Front. Mar. Sci., 9, 10.3389/fmars.2022.850207, 2022.

Soyam, P. S.: Black carbon aerosols over a semi-arid rain shadow location in Peninsular India: Temporal variability and sources, J. Earth Syst. Sci., 130, https://doi.org/10.1007/s12040-021-01610-5, 2021.

Sun, C., Adachi, K., Misawa, K., Cheung, H. C., Chou, C. C. K., and Takegawa, N.: Mixing state of black carbon particles in Asian outflow observed at a remote site in Taiwan in the spring of 2017, J. Geophys. Res. Atmos., 125, 13, https://doi.org/10.1029/2020jd032526, 2020a.

Sun, L., Chen, T., Jiang, Y., Zhou, Y., Sheng, L., Lin, J., Li, J., Dong, C., Wang, C., Wang, X., Zhang, Q., Wang, W., and Xue, L.: Ship emission of nitrous acid (HONO) and its impacts on the marine atmospheric oxidation chemistry, Sci. Total Environ., 735, 139355, https://doi.org/10.1016/j.scitotenv.2020.139355, 2020b.

Sun, Q., Liang, B., Cai, M., Zhang, Y., Ou, H., Ni, X., Sun, X., Han, B., Deng, X., Zhou, S., and Zhao, J.: Cruise observation of the marine atmosphere and ship emissions in South China Sea: Aerosol composition, sources, and the aging process,

849   Environ. Pollut., 316, 120539, https://doi.org/10.1016/j.envpol.2022.120539, 2023.

850 Sun, T., Wu, C., Wu, D., Liu, B., Sun, J. Y., Mao, X., Yang, H., Deng, T., Song, L., Li, M., Li, Y. J., and Zhou, Z.: Time-resolved

851   black carbon aerosol vertical distribution measurements using a 356-m meteorological tower in Shenzhen, Theor. Appl.

852   Climatol., 140, 1263-1276, https://doi.org/10.1007/s00704-020-03168-6, 2020c.

853 Taketani, F., Miyakawa, T., Takashima, H., Komazaki, Y., Pan, X., Kanaya, Y., and Inoue, J.: Shipborne observations of

854   atmospheric black carbon aerosol particles over the Arctic Ocean, Bering Sea, and North Pacific Ocean during September

855   2014, J. Geophys. Res. Atmos., 121, 1914-1921, https://doi.org/10.1002/2015jd023648, 2016.

856 Tóth, A., Hoffer, A., Nyirő-Kósa, I., Pósfai, M., and Gelencsér, A.: Atmospheric tar balls: aged primary droplets from biomass

857   burning?, Atmos. Chem. Phys., 14, 6669-6675, https://doi.org/10.5194/acp-14-6669-2014, 2014.

858 Ueda, S., Osada, K., Hara, K., Yabuki, M., Hashihama, F., and Kanda, J.: Morphological features and mixing states of soot-

859   containing particles in the marine boundary layer over the Indian and Southern oceans, Atmos. Chem. Phys., 18, 9207-9224,

860   https://doi.org/10.5194/acp-18-9207-2018, 2018.

861 Virkkula, A.: Modeled source apportionment of black carbon particles coated with a light-scattering shell, Atmos. Meas. Tech.,

862   14, 3707-3719, https://doi.org/10.5194/amt-14-3707-2021, 2021.

863 Wang, G., Chen, J., Xu, J., Yun, L., Zhang, M., Li, H., Qin, X., Deng, C., Zheng, H., Gui, H., Liu, J., and Huang, K.:

864   Atmospheric processing at the sea-land interface over the South China Sea: Secondary aerosol formation, aerosol acidity,

865   and role of sea salts, J. Geophys. Res. Atmos., 127, https://doi.org/10.1029/2021jd036255, 2022.

866 Wang, Q., Liu, H., Ye, J., Tian, J., Zhang, T., Zhang, Y., Liu, S., and Cao, J.: Estimating absorption Ångström exponent of

867   black carbon aerosol by coupling multiwavelength absorption with chemical composition, Environ. Sci. Technol., 8, 121-

868   127, https://doi.org/10.1021/acs.estlett.0c00829, 2020a.

869 Wang, Q., Liu, H., Wang, P., Dai, W., Zhang, T., Zhao, Y., Tian, J., Zhang, W., Han, Y., and Cao, J.: Optical source

870   apportionment and radiative effect of light-absorbing carbonaceous aerosols in a tropical marine monsoon climate zone:

871   The importance of ship emissions, Atmos. Chem. Phys., 20, 15537-15549, https://doi.org/10.5194/acp-20-15537-2020,

872   2020b.

873 Wang, Y., Liu, F., He, C., Bi, L., Cheng, T., Wang, Z., Zhang, H., Zhang, X., Shi, Z., and Li, W.: Fractal dimensions and mixing

874   structures of soot particles during atmospheric processing, Environ. Sci. Technol., 4, 487-493,

875   https://doi.org/10.1021/acs.estlett.7b00418, 2017.

876 Wang, Y. L. and Wu, C. R.: Nonstationary El Nino teleconnection on the post-summer upwelling off Vietnam, Sci. Rep., 10,

877   13319, https://doi.org/10.1038/s41598-020-70147-2, 2020.

878 Wei, X., Zhu, Y., Hu, J., Liu, C., Ge, X., Guo, S., Liu, D., Liao, H., and Wang, H.: Recent progress in impacts of mixing state

879   on optical properties of black carbon aerosol, Curr. Pollut. Rep., 6, 380-398, https://doi.org/10.1007/s40726-020-00158-0,

880   2020.

881 Wu, D., Wu, C., Liao, B., Chen, H., Wu, M., Li, F., Tan, H., Deng, T., Li, H., Jiang, D., and Yu, J. Z.: Black carbon over the

882   South China Sea and in various continental locations in South China, Atmos. Chem. Phys., 13, 12257-12270,

883   https://doi.org/10.5194/acp-13-12257-2013, 2013a.

884 Wu, H., Lattuada, M., and Morbidelli, M.: Dependence of fractal dimension of DLCA clusters on size of primary particles,

885   Adv. Colloid Interface Sci., 195-196, 41-49, https://doi.org/10.1016/j.cis.2013.04.001, 2013b.

886 Xing, J., Bian, L., Hu, Q., Yu, J., Sun, C., and Xie, Z.: Atmospheric black carbon along a cruise path through the Arctic Ocean
887   during the fifth Chinese Arctic Research Expedition, Atmosphere, 5, 292-306, https://doi.org/10.3390/atmos5020292, 2014.

888 Yan, J., Chen, L., Zhao, S., Zhang, M., Lin, Q., and Li, L.: Impact of marine and continental sources on aerosol characteristics
889   using an on-board SPAMS over southeast sea, China, Environ. Sci. Pollut. Res., 25, 30659-30670,
890   https://doi.org/10.1007/s11356-018-2902-5, 2018.

891 Yang, M., Howell, S. G., Zhuang, J., and Huebert, B. J.: Attribution of aerosol light absorption to black carbon, brown carbon,
892   and dust in China – interpretations of atmospheric measurements during EAST-AIRE, Atmos. Chem. Phys., 9, 2035-2050,
893   https://doi.org/10.5194/acp-9-2035-2009, 2009.

894 You, R., Radney, J. G., Zachariah, M. R., and Zangmeister, C. D.: Measured wavelength-dependent absorption enhancement
895   of internally mixed black carbon with absorbing and nonabsorbing materials, Environ. Sci. Technol., 50, 7982-7990,
896   https://doi.org/10.1021/acs.est.6b01473, 2016.

897 Yu, G.-H., Park, S., Shin, S.-K., Lee, K.-H., and Nam, H.-G.: Enhanced light absorption due to aerosol particles in ship plumes
898   observed at a seashore site, Atmos. Pollut. Res., 9, 1177-1183, https://doi.org/10.1016/j.apr.2018.05.005, 2018.

899 Yus-Díez, J., Bernardoni, V., Močnik, G., Alastuey, A., Ciniglia, D., Ivančič, M., Querol, X., Perez, N., Reche, C., Rigler, M.,
900   Vecchi, R., Valentini, S., and Pandolfi, M.: Determination of the multiple-scattering correction factor and its cross-sensitivity
901   to scattering and wavelength dependence for different AE33 Aethalometer filter tapes: A multi-instrumental approach,
902   Atmos. Meas. Tech., 14, 6335-6355, https://doi.org/10.5194/amt-14-6335-2021, 2021.

903 Zefirov, V. V., Elmanovich, I. V., Levin, E. E., Abramchuk, S. S., Kharitonova, E. P., Khokhlov, A. A., Kondratenko, M. S.,
904   and Gallyamov, M. O.: Synthesis of manganese oxide electrocatalysts in supercritical carbon dioxide, J. Mater. Sci., 53,
905   9449-9462, https://doi.org/10.1007/s10853-018-2242-3, 2018.

906 Zhang, K., Allen, G., Yang, B., Chen, G., Gu, J., Schwab, J. J., Felton, D., and Rattigan, O.: Joint measurements of PM2.5 and
907   light-absorptive PM in woodsmoke-dominated ambient and plume environments, Atmos. Chem. Phys., 17, 11441-11452,
908   https://doi.org/10.5194/acp-17-11441-2017, 2017.

909 Zhang, X., Trzepla, K., White, W., Raffuse, S., and Hyslop, N. P.: Intercomparison of thermal–optical carbon measurements
910   by Sunset and Desert Research Institute (DRI) analyzers using the IMPROVE_A protocol, Atmos. Meas. Tech., 14, 3217-
911   3231, https://doi.org/10.5194/amt-14-3217-2021, 2021.

912 Zhu, J., Crozier, P. A., and Anderson, J. R.: Characterization of light-absorbing carbon particles at three altitudes in East Asian
913   outflow by transmission electron microscopy, Atmos. Chem. Phys., 13, 6359-6371, https://doi.org/10.5194/acp-13-6359-
914   2013, 2013.

915 Zotter, P., Herich, H., Gysel, M., El-Haddad, I., Zhang, Y., Močnik, G., Hüglin, C., Baltensperger, U., Szidat, S., and Prévôt,
916   A. S. H.: Evaluation of the absorption Ångström exponents for traffic and wood burning in the Aethalometer-based source
917   apportionment using radiocarbon measurements of ambient aerosol, Atmos. Chem. Phys., 17, 4229-4249,
918   https://doi.org/10.5194/acp-17-4229-2017, 2017.

919

920

921   **Table 1.** Classification of the campaign period during May 05–June 09, 2021.

Name	Date	Cruise route	Monsoon	Wind direction
BMP-1	May 05–09	AB	before	0–90°, northeast
BMP-2	May 10–22	B→C→D	before	90–180°, southeast
BMP-3	May 23–26	D→E	before	around 180°, southeast
TMP	May 27–Jun 01	EB	transition	around 180°, south
AMP	June 02–09	B→D→A	after	180–270°, southwest
SPP*	Screened	Screened	N/A	Screened

922   * Ship pollution period is screened based on BC concentration and relative wind direction as mentioned in the method section.

923

924   **Table 2.** Source apportionment of BC based on the two-component AAE model.

Period	a.BC(FF)[*] (μg m^{-3})	a.BC(BB)[*] (μg m^{-3})	r.BC(BB)[*] (μg m^{-3})	r.BC(FF)[*] (μg m^{-3})	f.BC(FF)[*] (%)	f.BC(BB)[*] (%)
BMP	0.2 ± 0.1	0.08 ± 0.06	0–0.9	0–0.3	77.9 ± 5.8	22.1 ± 5.8
TMP	0.2 ± 0.3	0.06 ± 0.1	0.02–1.8	0–1.1	82.2 ± 6.2	17.8 ± 6.2
AMP	0.2 ± 0.1	0.05 ± 0.05	0.01–0.9	0–0.3	80.8 ± 4.0	19.2 ± 4.0
SPP	4.4 ± 5.7	0.7 ± 0.9	0.2–32.8	0.04–10.3	83.0 ± 6.7	17.0 ± 6.7
Bio. [**]	0.8 ± 0.3	0.8 ± 0.4	0.05–1.2	0–1.5	58.1 ± 16.7	41.9 ± 16.7

925   [*] a represents average, r for range, f for fraction;

926   [**] Bio. stands for the two biomass burning events as noted in the main text.

927

928 **Table 3.** Summary of AAE values, mass concentrations, and the relevant fractions for the BC particles in $PM_{2.5}$ from coast site

929 and cruise measurements using the AE series aethalometer.

Region	Time	AAE values (at wavelengths, nm)	BC avg. conc. ($\mu g\ m^{-3}$)	Fraction (%)	Reference
East China Sea[c]	May, 2017	0.9–1.3 (370–950)	0.8–3.6	2.5–11 or 45–60 for BrC	(Yu et al., 2018)
Central Adriatic[c]	Feb.–Jul., 2019	1.25–1.49 (470/950)	0.57 ± 0.64	79 for BC(FF) 21 for BC(BB)	(Milinković et al., 2021)
Bay of Bengal[c, n]	Dec., 2008–Jan., 2009	1.81–1.98 (370–950)	5.1 ± 3.0[c]; 2.5 ± 1.4[n]	<10 for BC(FF) >85 for BC(BB)	(Kedia et al., 2012)
South China Sea[n]	Sep.–Oct. 2019	-	1.9 ± 0.4	-	(Wang et al., 2022)
South China Sea[c]	Dec. 2017	1.2–1.5 (375/880)	6.6–4.9	-	(Sun et al., 2020c)
South China Sea[n]	May–Jun. 2021	1.02–1.14 or 1.93 (370–950)	0.33 ± 0.38	78–82 for BC(FF) 18–22 for BC(BB) BB events: 58 for BC(FF) 42 for BC(BB)	This study

930 [c] coastal site measurement;

931 [n] cruise (remote) measurement.

932

933

934
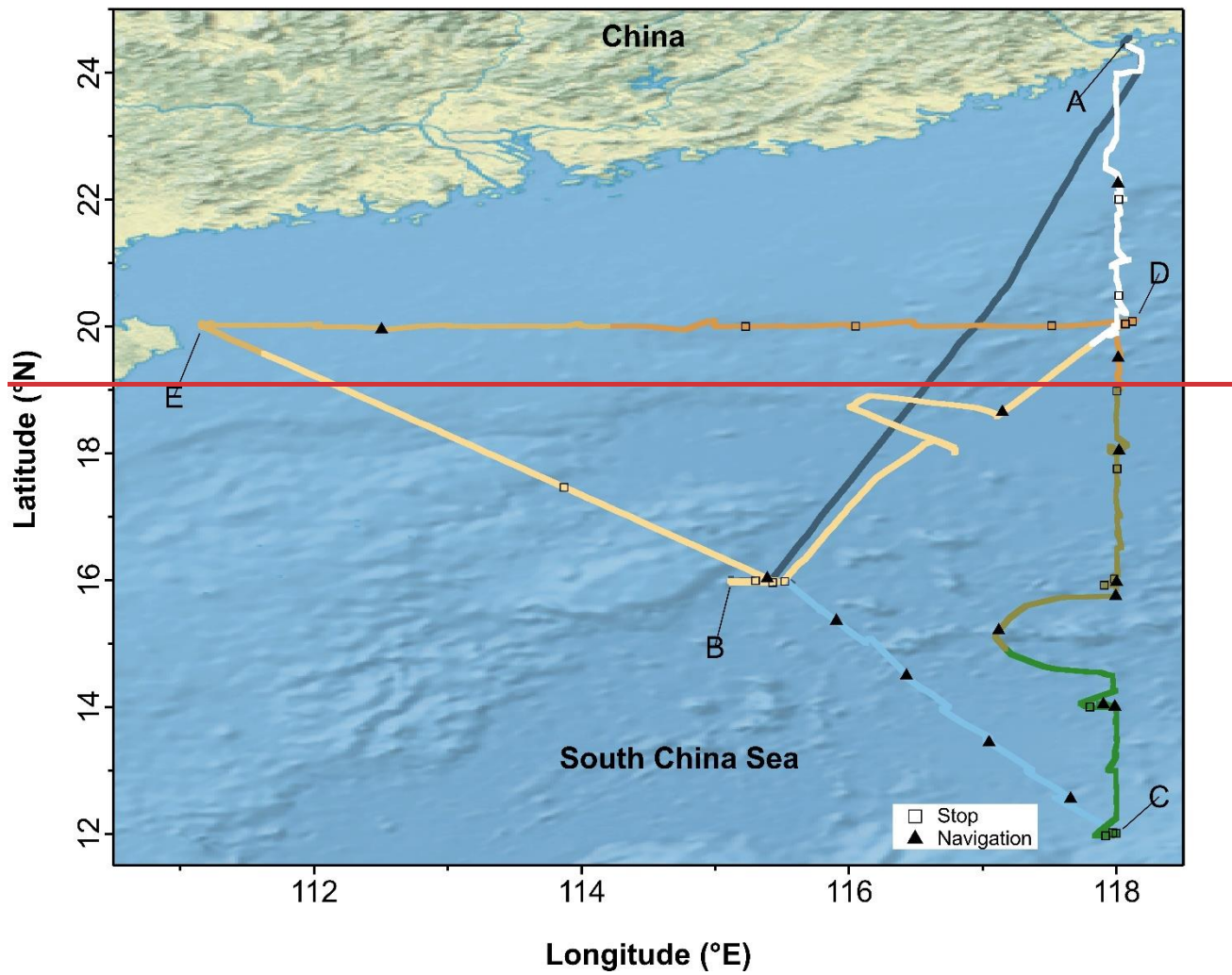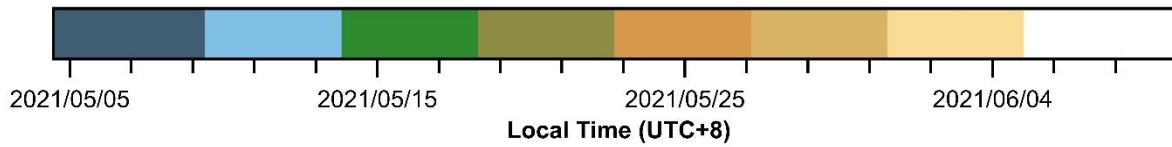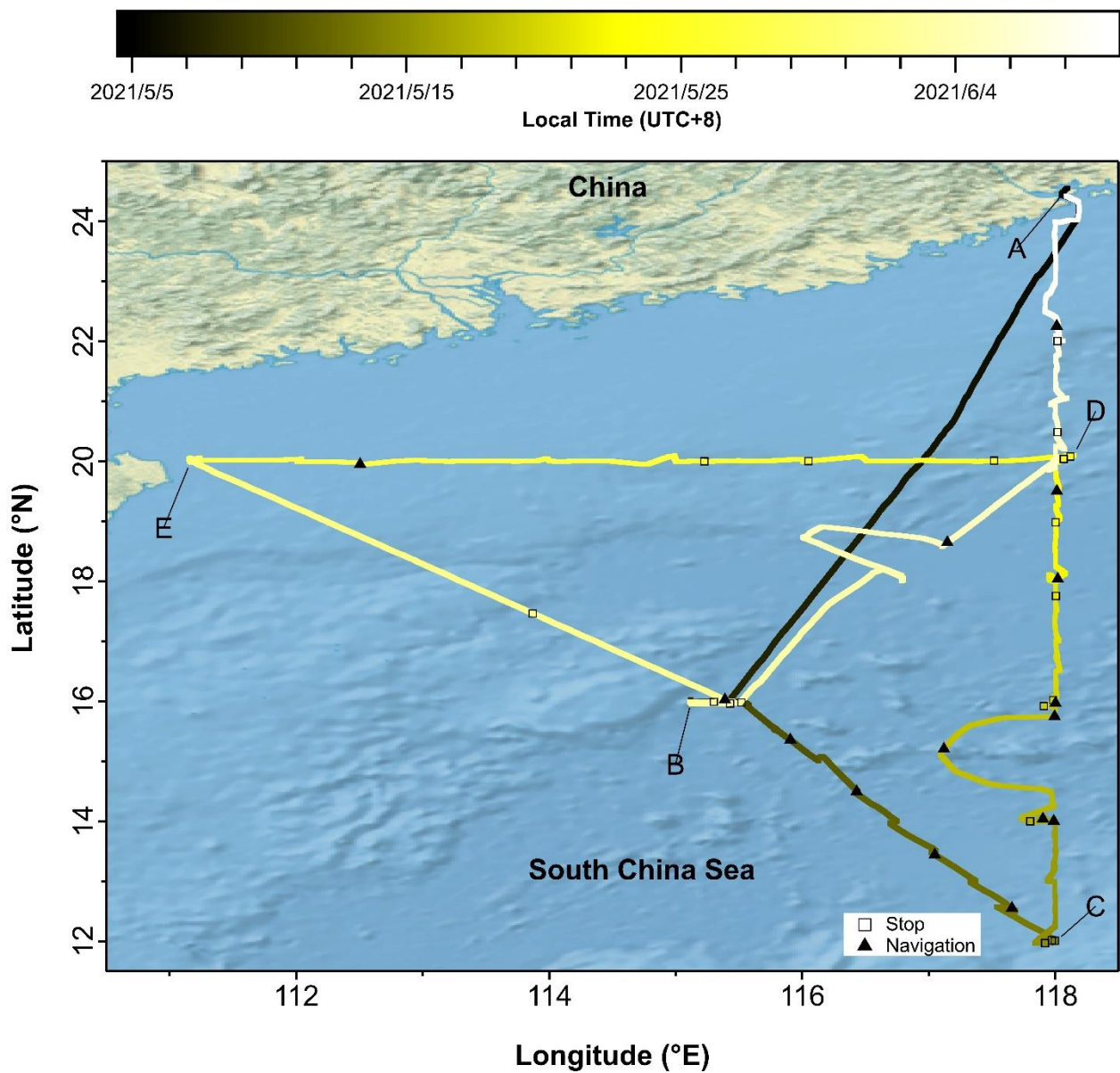
938 ~~Figure 1. Map of the cruise route for the campaign in the South China Sea during May 05- Jun 9, 2021. The ship route is dated by~~

939 ~~the intensity bar at the top. The open squares and solid triangles indicate the single particle sampling location, collected during stop~~

940 ~~and navigation, respectively.~~

941

942

943
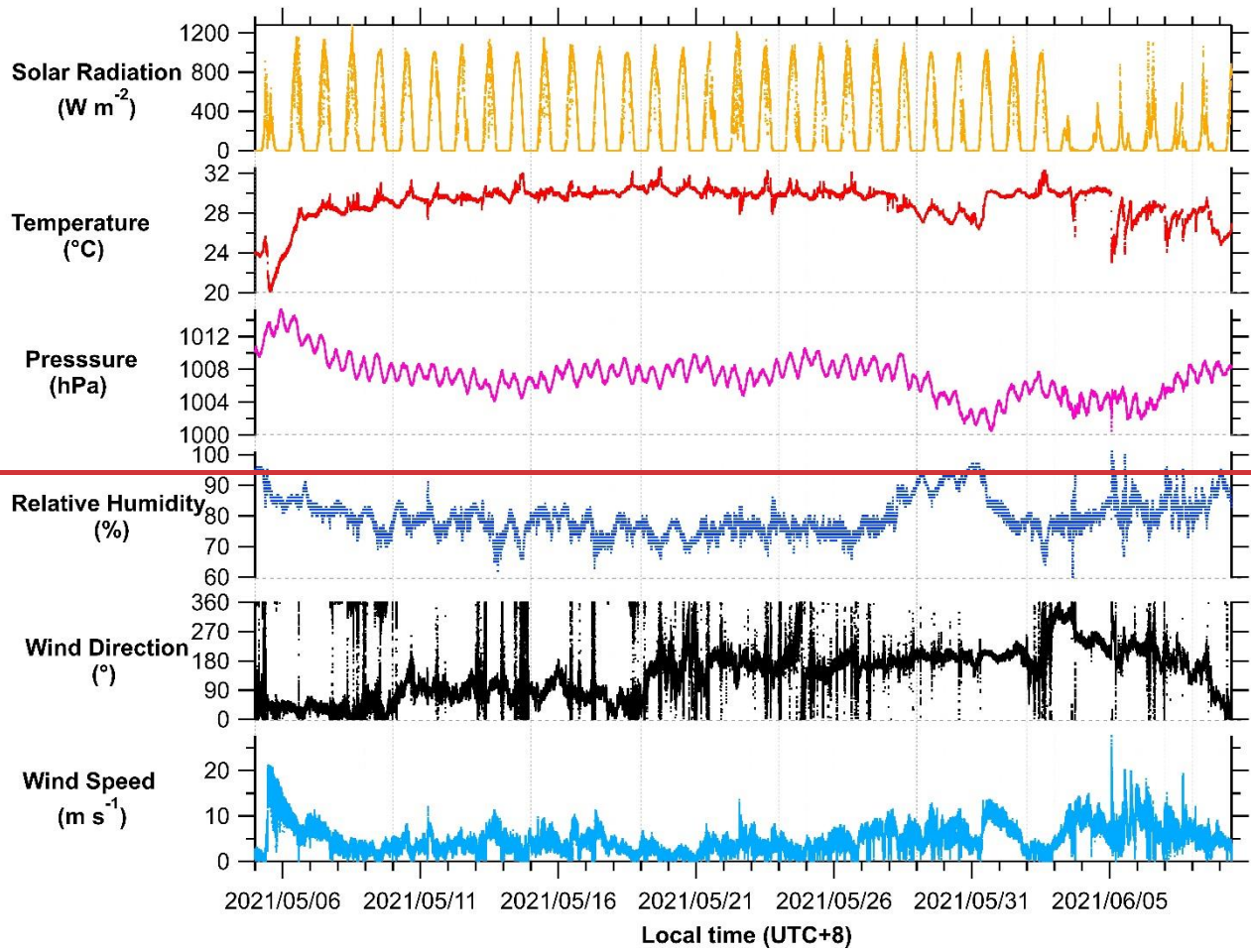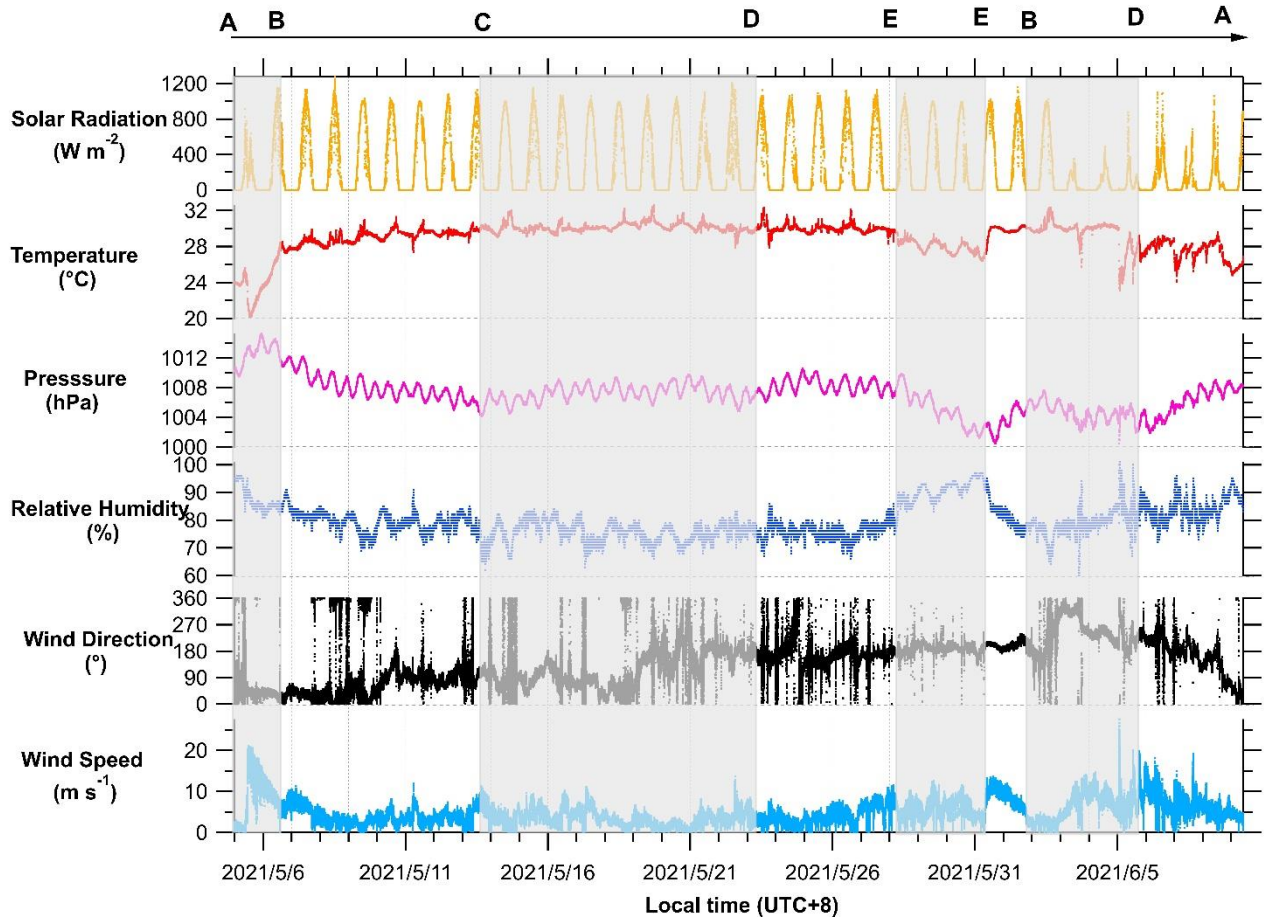
944

945

946 **Figure 2. Time series of meteorological variables of solar radiation (SR), temperature, pressure, relative humidity (RH), wind**

947 **direction (WD), and wind speed (WS) during the campaign. The time resolution is 1 min for all the data except for WS and WD (3**

948 **sec). All data points are shown in dots style. The shaded and unshaded areas sequentially indicate the cruise routes from AB, B to**

949 **C, C to D, D to E, E to E (ship stop), E to B, B to D, and D to A, as marked in the Figure 1.**

950 ~~Figure 2. Time series of meteorological variables of solar radiation (SR), temperature, pressure, relative humidity (RH), wind~~

951 ~~direction (WD), and~~ ~~wind speed (WS) during the campaign. The time resolution is 1 min for all the data except for WS and WD (3~~

952 ~~sec). All data points are shown in dots style.~~

953
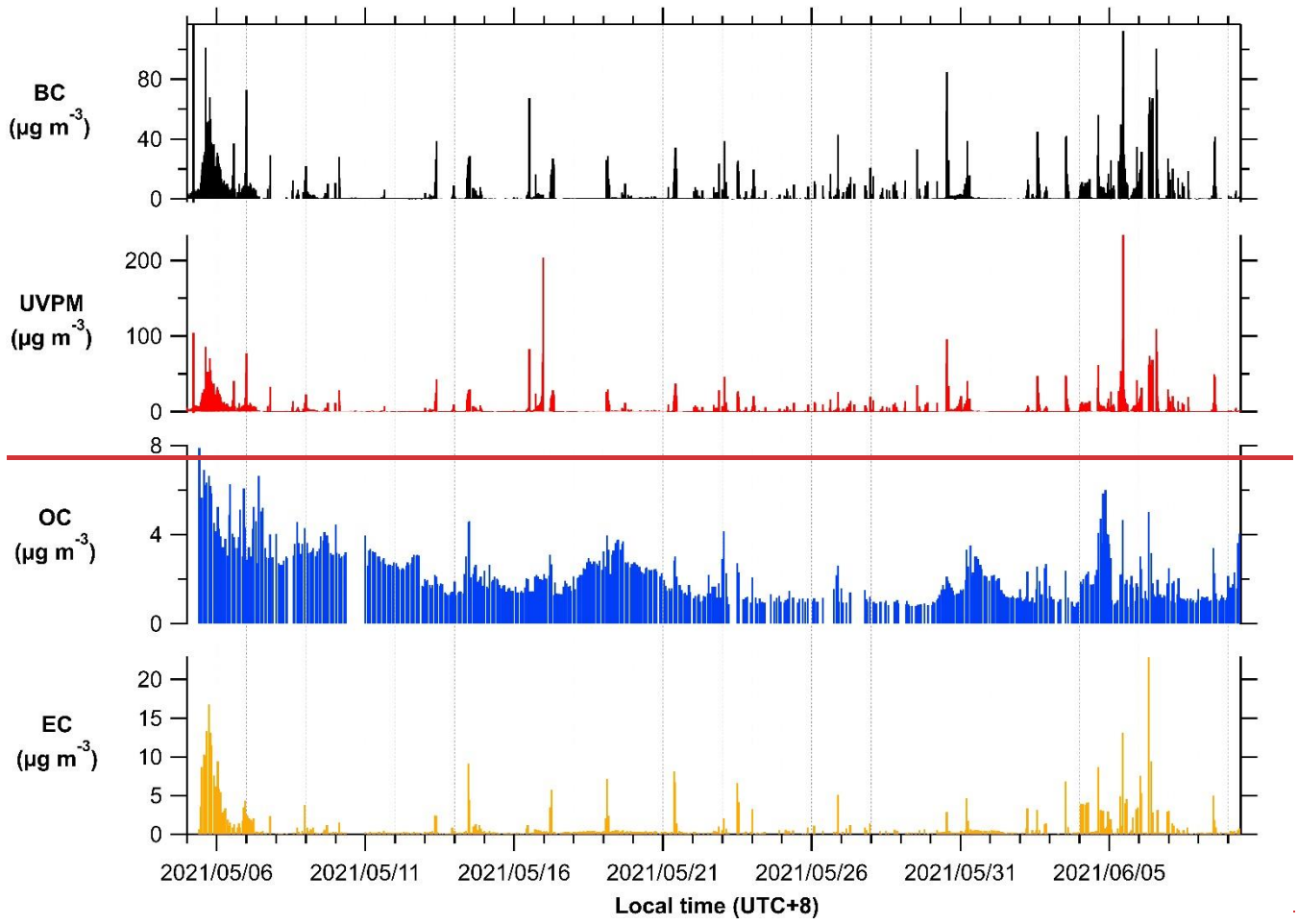
954
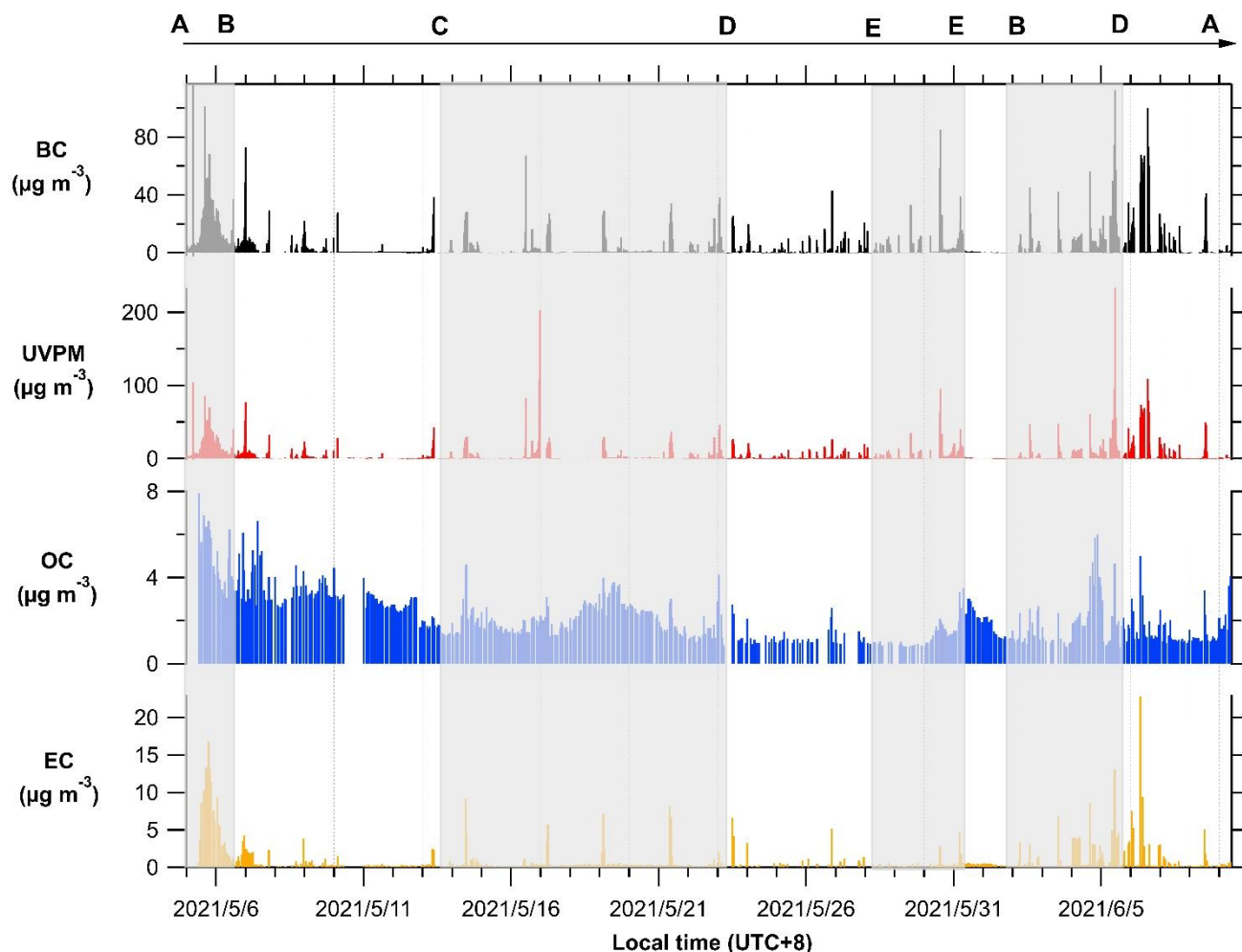
955

Figure 3. Time series of the mass concentration of black carbon (BC), ultraviolet particle matter (UVPM), organic carbon (OC)

and elemental carbon (EC) in PM2.5 during the campaign. The time resolution is 1 min for all the data except for OC and EC (1 h).

All data points are shown in stick-to-zero style. The shaded and unshaded areas sequentially indicate the cruise routes from AB, B

to C, C to D, D to E, E to E (ship stop), E to B, B to D, and D to A, as marked in the Figure 1.

~~Figure 3. Time series of the mass concentration of black carbon (BC), ultraviolet particle matter (UVPM), organic carbon (OC)~~
~~and elemental carbon (EC) in PM2.5 during the campaign. The time resolution is 1 min for all the data except for OC and EC (1 h).~~
~~All data points are shown in stick-to -to-zero style.~~

Figure 4. The time series of fire spots distribution and the 72-h backward trajectories over the South China Sea (SCS) during the campaign. The solid circles were dated by the intensity bar at the top, representing the detected fire spots using MODIS satellite with a confidence threshold of >80%. The light grey, grey and black 72-h backward trajectories were obtained at AGL heights of 100, 500 and 1000 m using the HYSPLIT model.

968

969
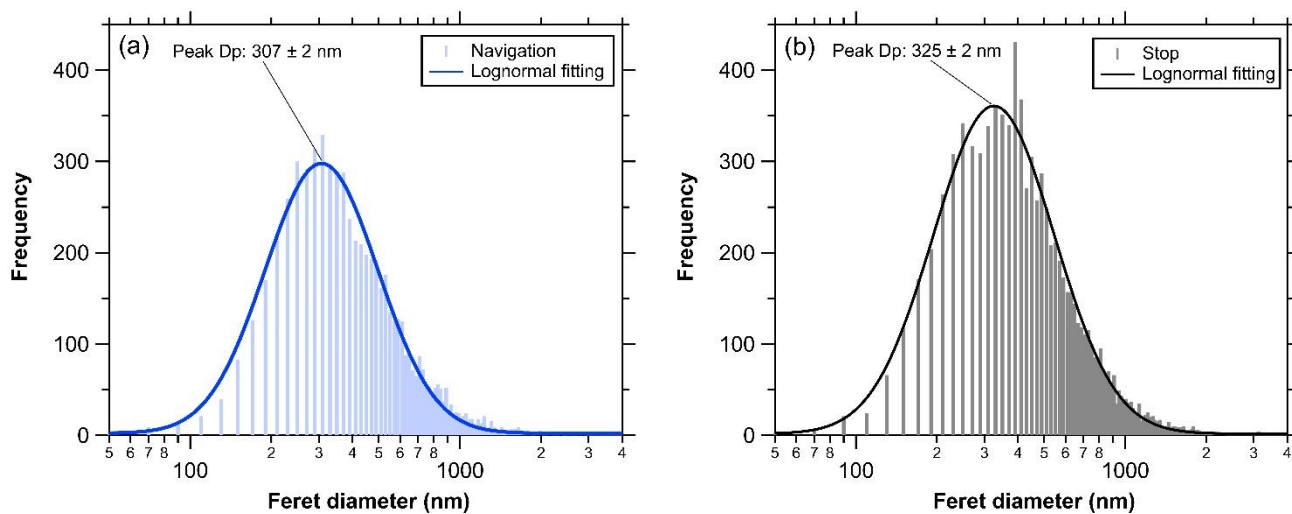
Figure 5Figure 4. Lognormal fitting of particle size distribution using Feret diameter determined from the TEM images with the ImageJ analysis during navigation (a) and stop (b). The histograms are set with a bin starting at 50 nm, a bin width of 20 nm, and a total bin number of 200.

973

974

975

976

977

978

979

980
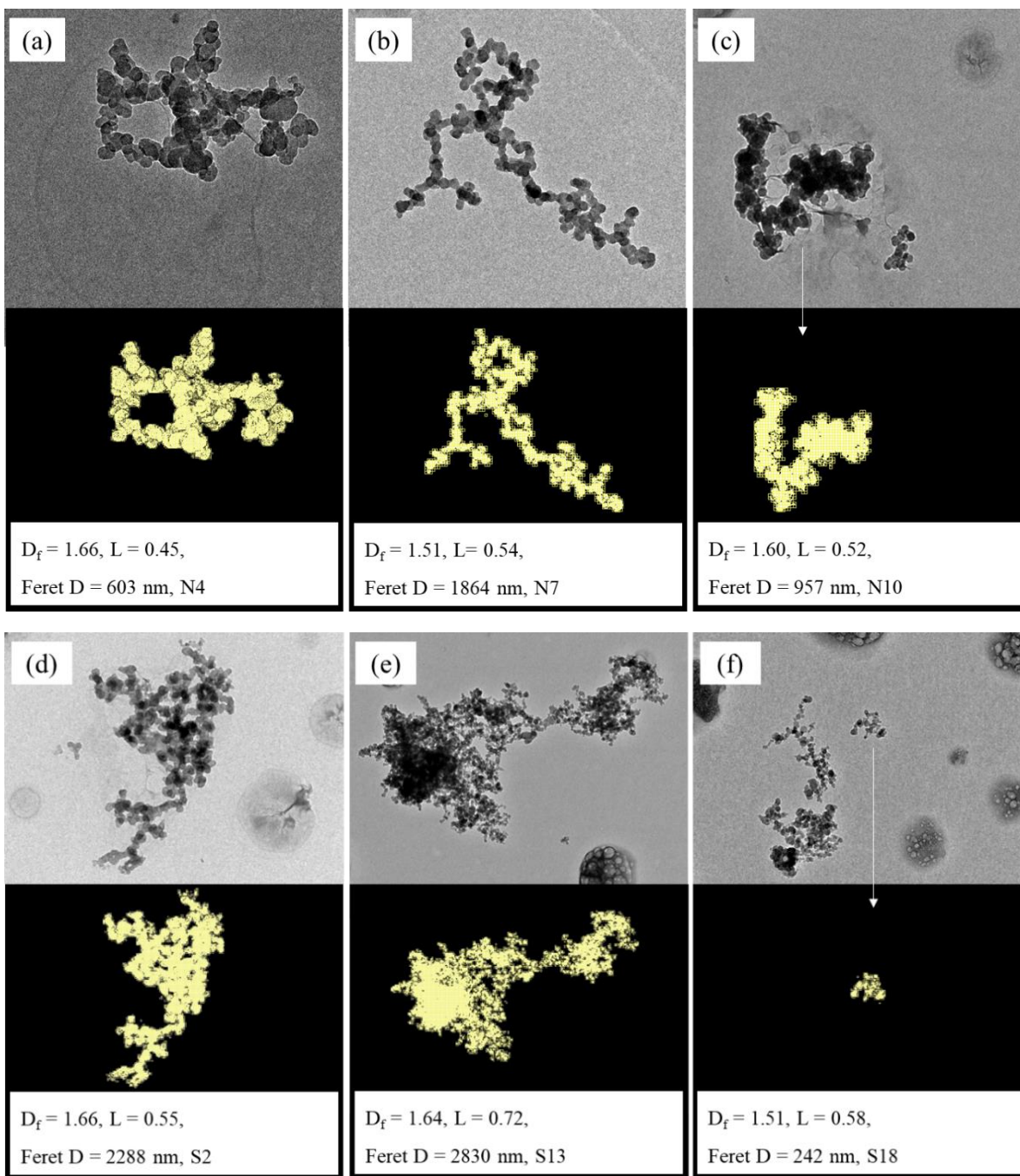
Figure 6Figure 5. Examples of the BC TEM images and their corresponding Feret diameter (D), fractal dimension (D_f) and Lacunarity (L) based on the boxing counting method from the fractal analysis: (a-c) BC particles collected during navigation and (d-f) during stop. More sampling information can be found in Table S1 of SI (serial numbers N4, N7, N10, S2, S13, S18, etc.).

984

48

985
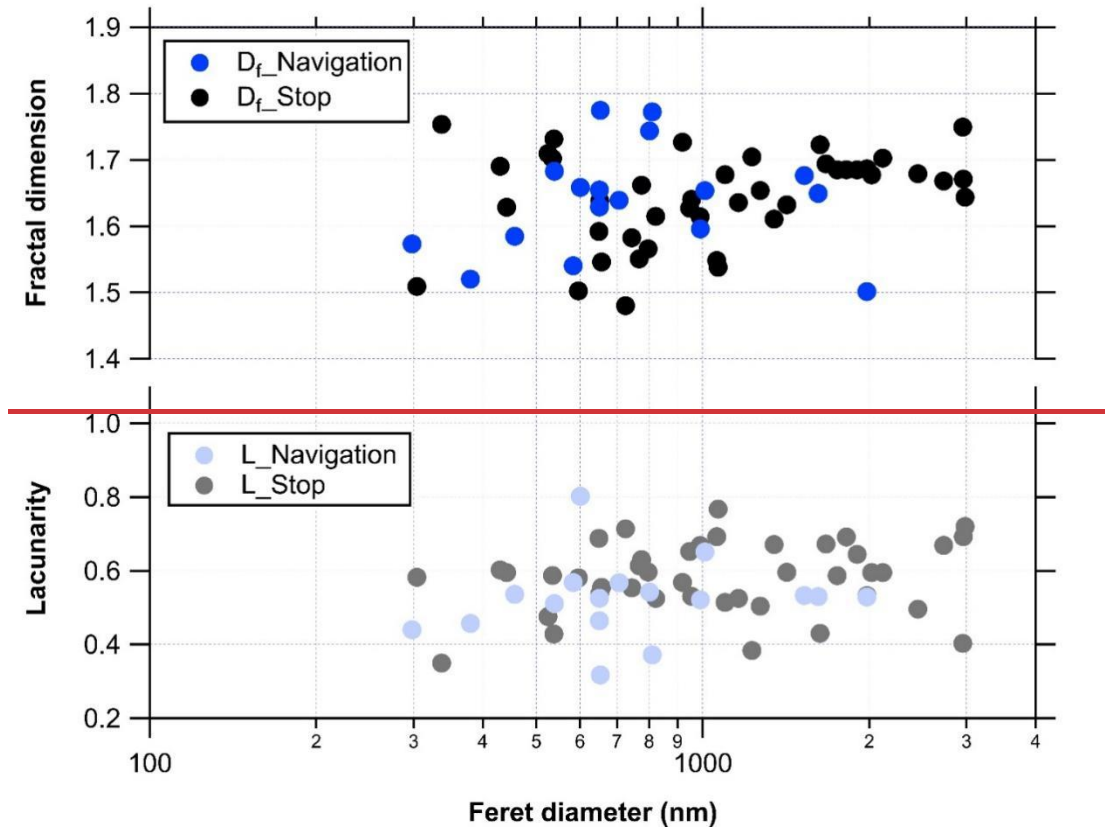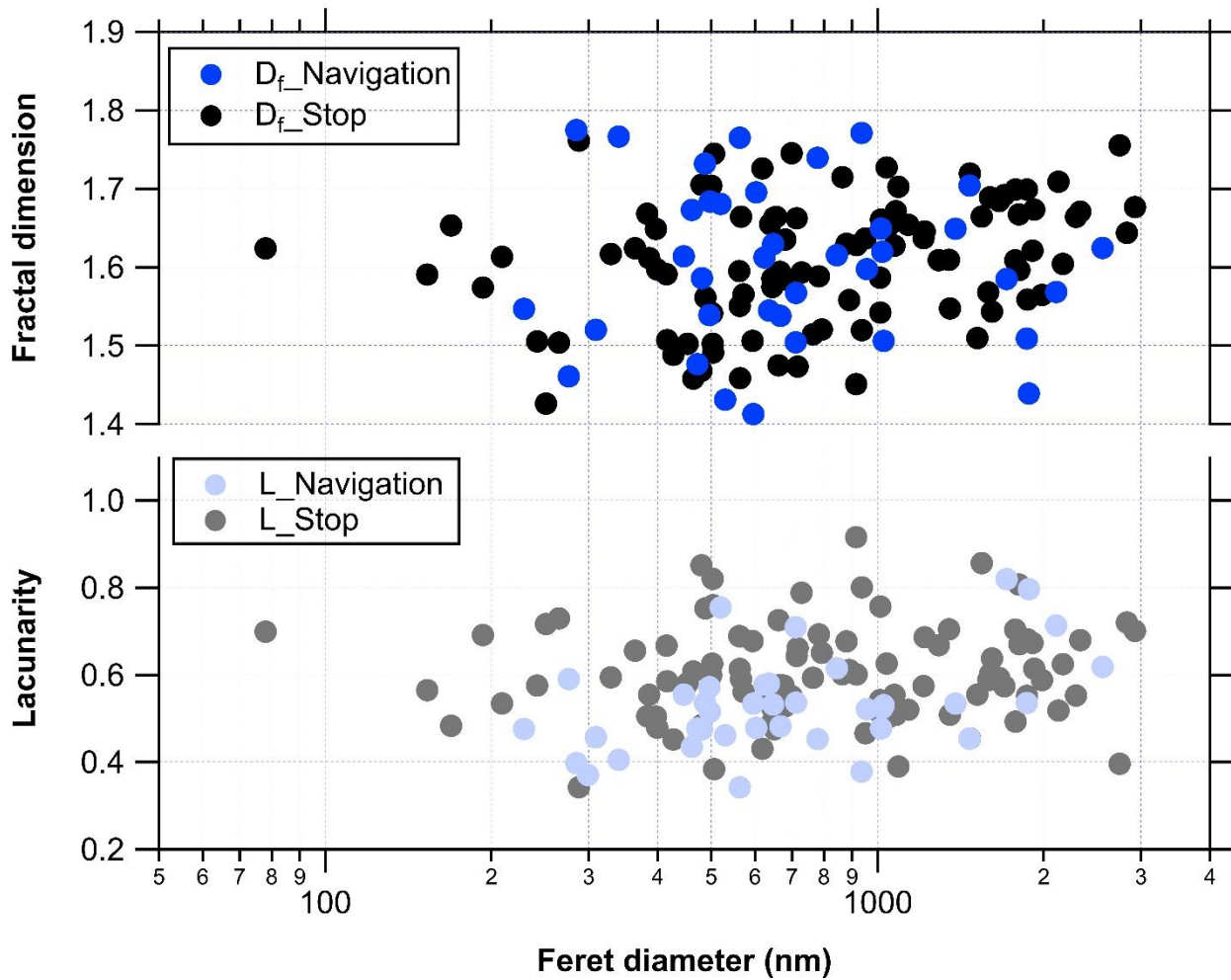
Figure 7. The size-dependent fractal dimension (D$_f$) and lacunarity (L) for each BC particle during navigation and stop. A total

987 **number of 134 data points are shown in Figure 6.**

988 ~~Figure 6. The size-dependent fractal dimension (D$_f$) and lacunarity (L) for each BC particle during navigation and stop.~~

989

990
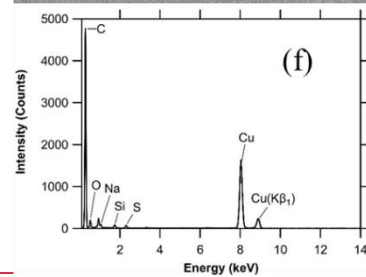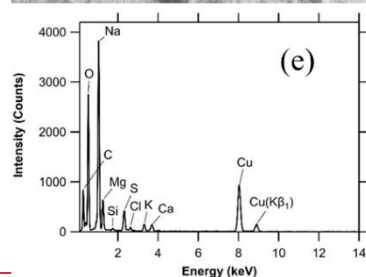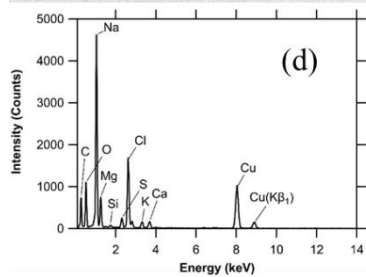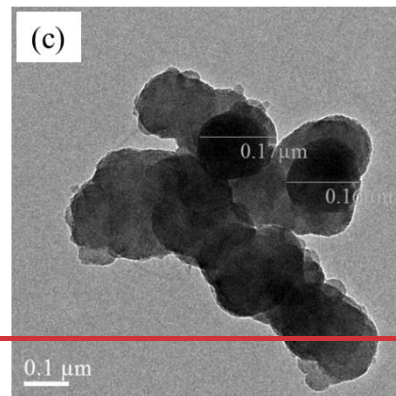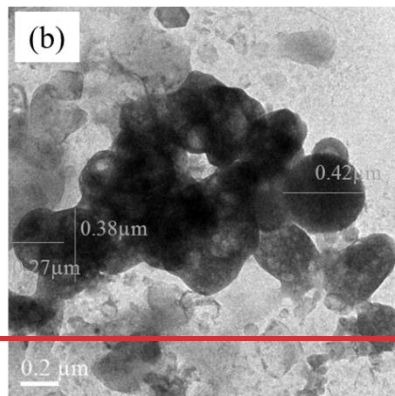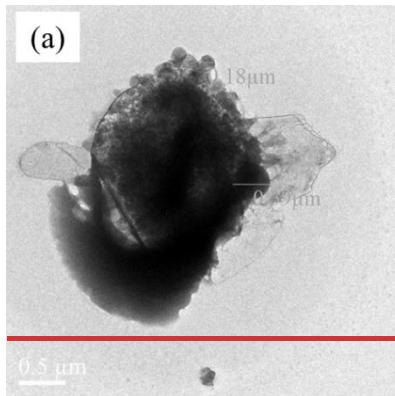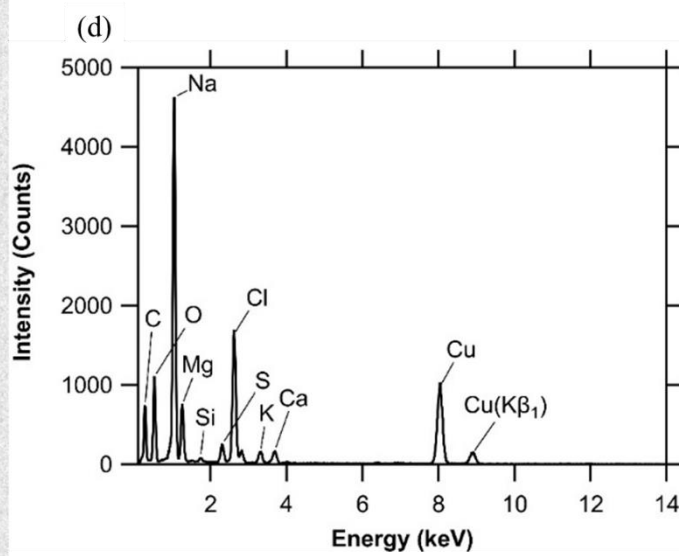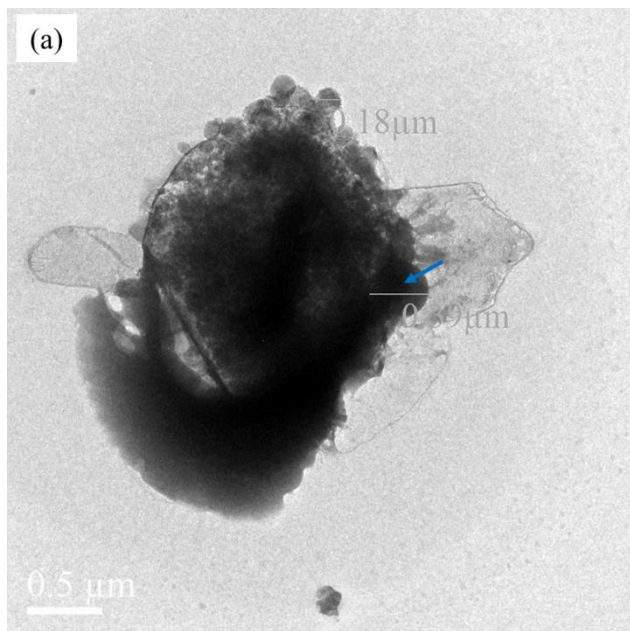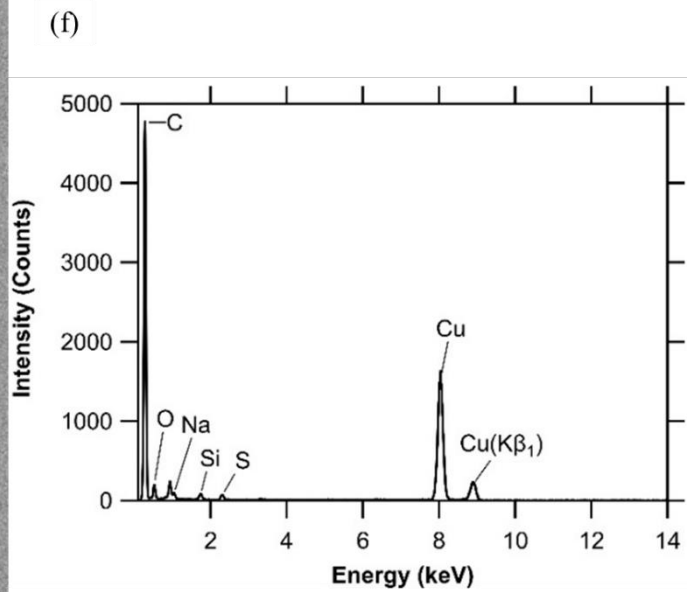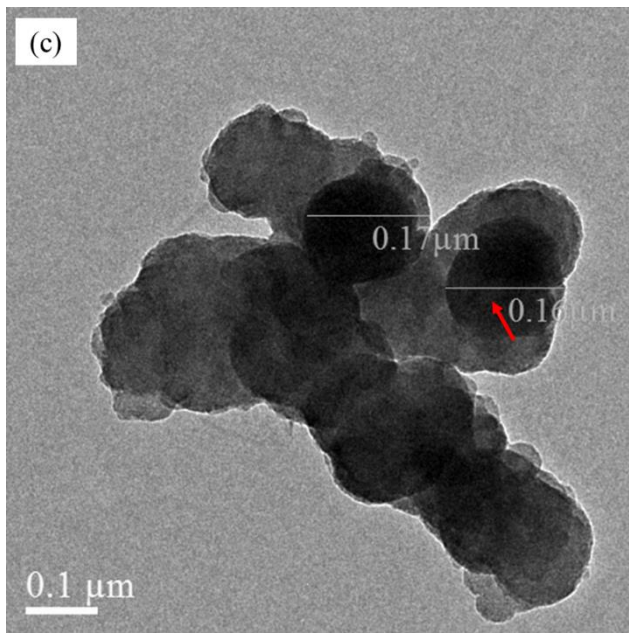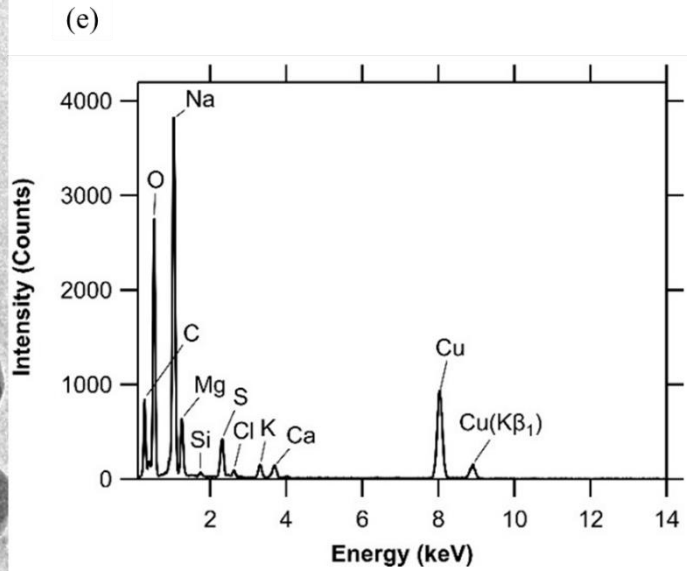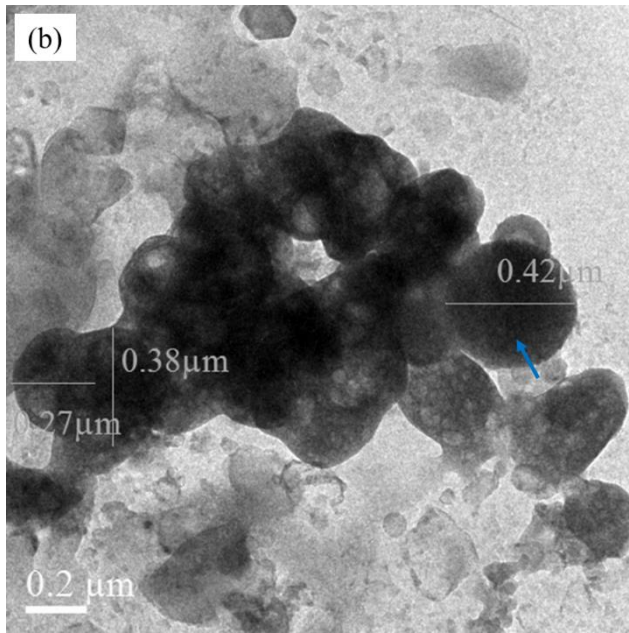
Figure 8. The example TEM images and their corresponding EDS spectra of particles collected during navigation: tar balls mixed with sea salt (a, d) at 8:55 on May 27, tar balls mixed with OC, sulfate (b, e), and amorphous carbon agglomerates mixed with sulfate (c, f) at 18:07 on Jun 01. The EDS spectra were collected by focusing the electron beam in the TEM and the illuminated area

996 covers the center of the particle for elemental analysis. The blue arrows indicate tar balls and the red arrow indicates amorphous

997 carbon. The EDS is obtained from beam focus on the center of the particle.

998 Figure 7. The example TEM images and their corresponding EDS spectra of tar ball particles collected during navigation: tar balls

999 mixed with sea salt (a, d) at 8:55 on May 27, tar balls mixed with OC, sulfate (b, e), and tar balls mixed with sulfate (e, f) at 18:07

1000 on Jun 01. The EDS spectra were collected by focusing the electron beam in the TEM and the illuminated area covers the particle

1001 for elemental analysis.
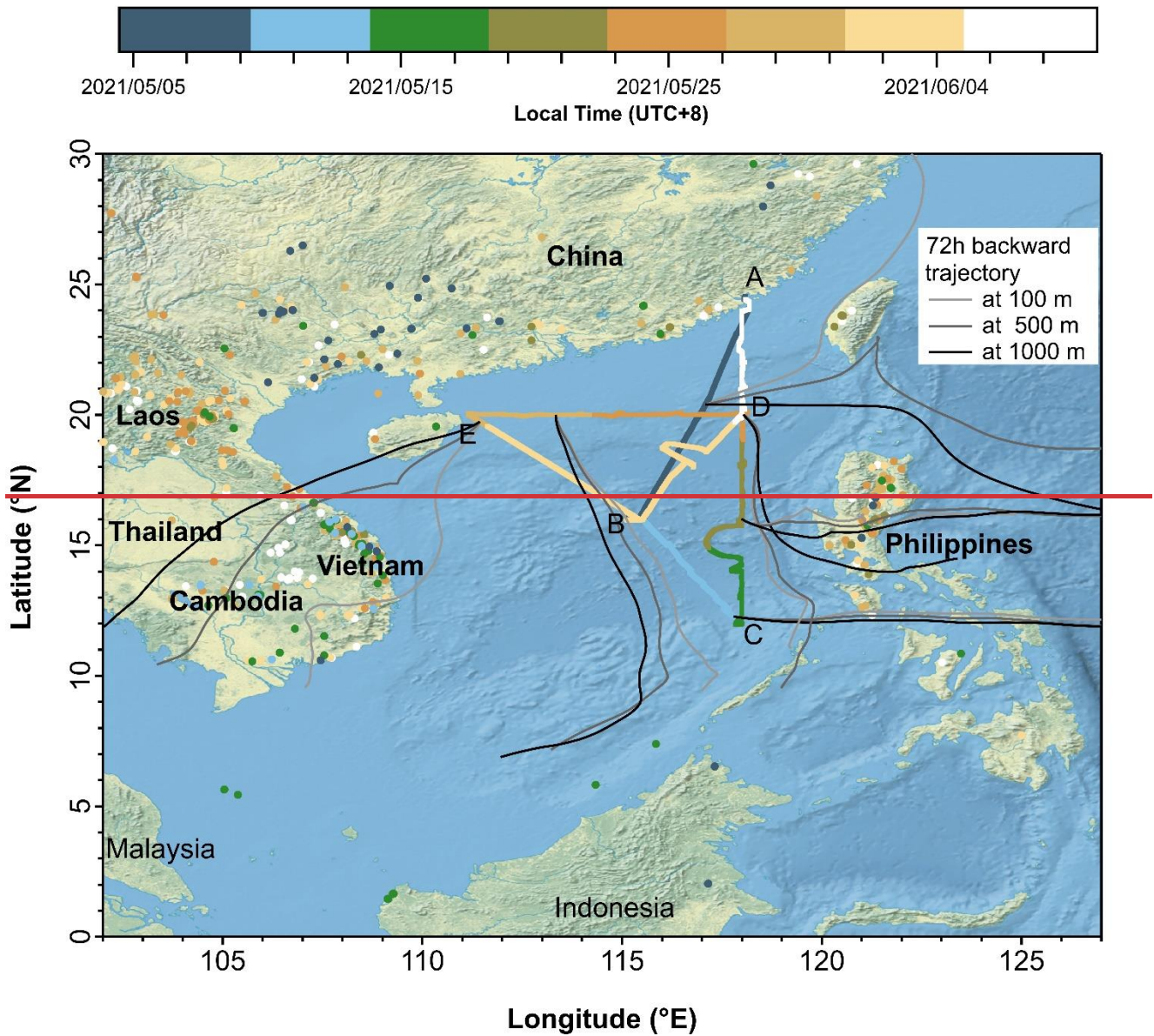
Figure 8. The time series of fire spots distribution and the 72-h backward trajectories over the South China Sea (SCS) during the campaign. The solid circles were dated by the intensity bar at the top, representing the detected fire spots using MODIS satellite with a confidence threshold of >80%. The light grey, grey and black 72-h backward trajectories were obtained at AGL heights of 100, 500 and 1000 m using the HYSPLIT model.

(a) BMP

(b) TMP

55

(c) AMP
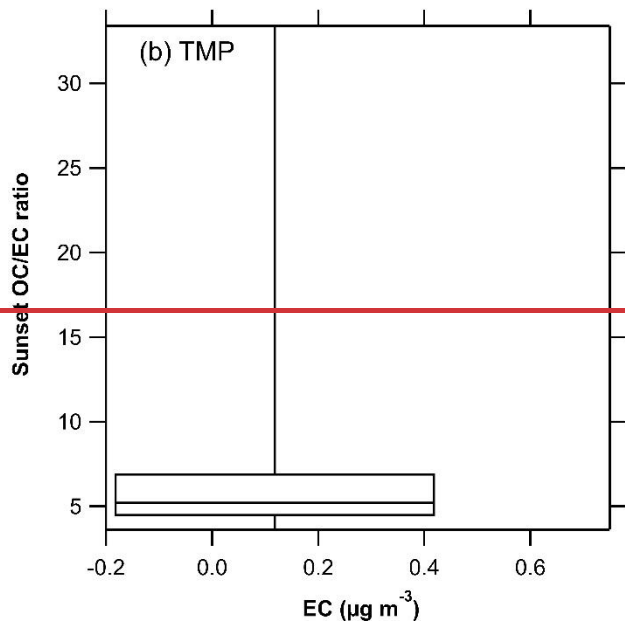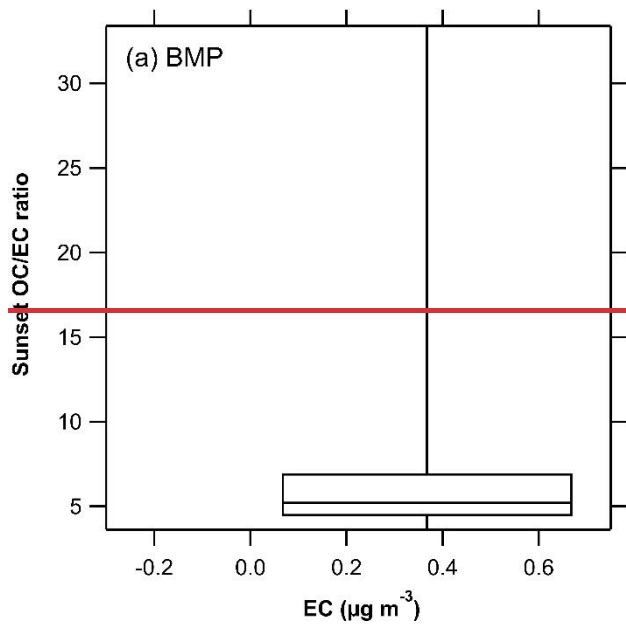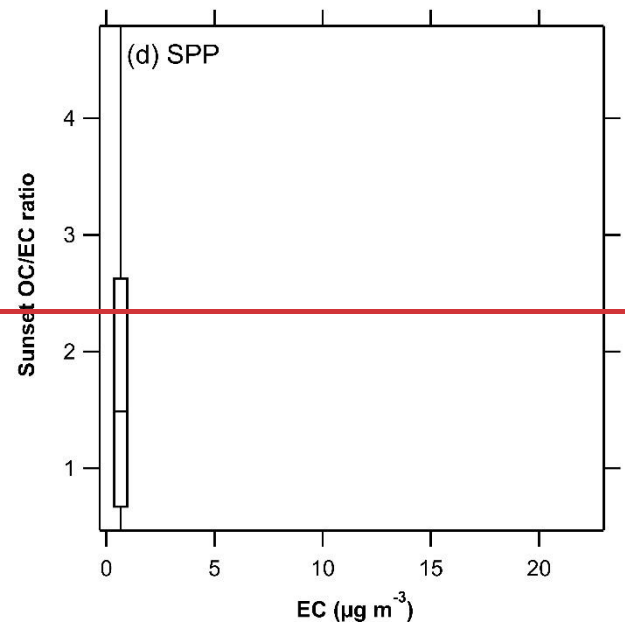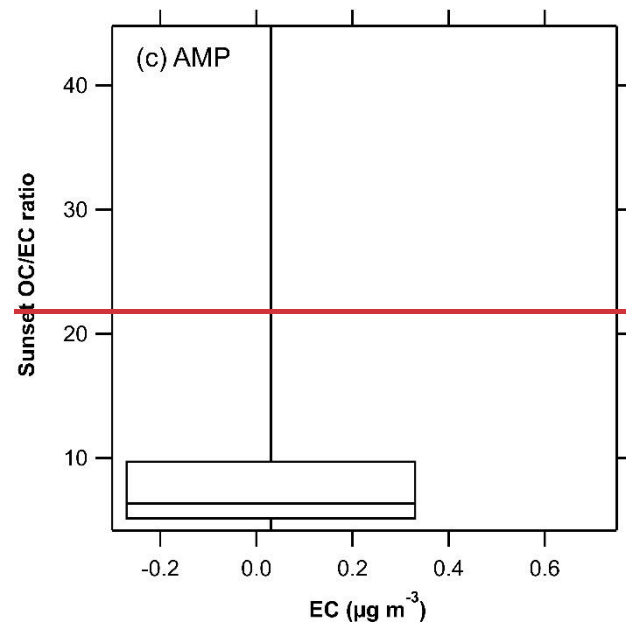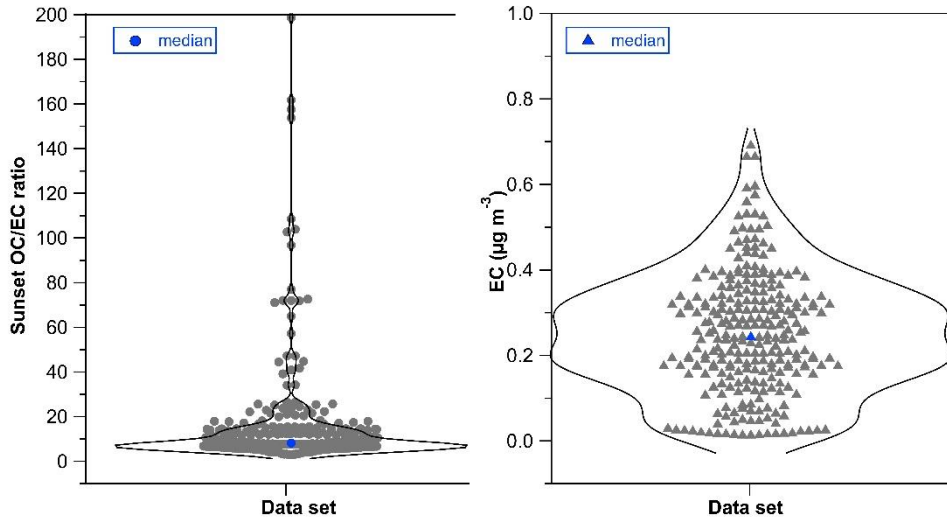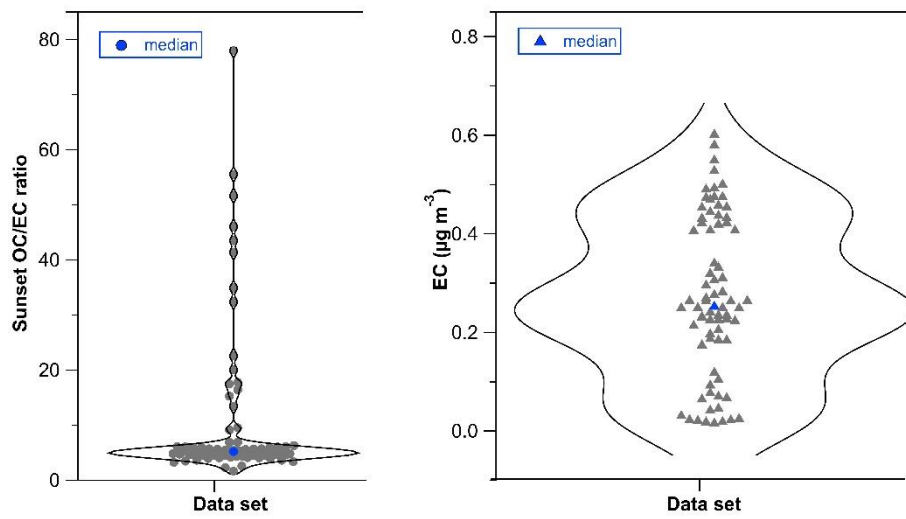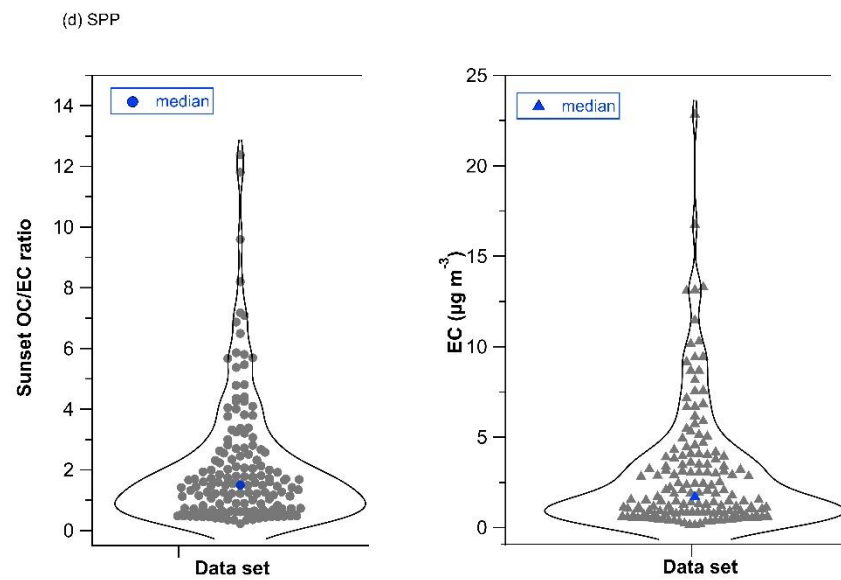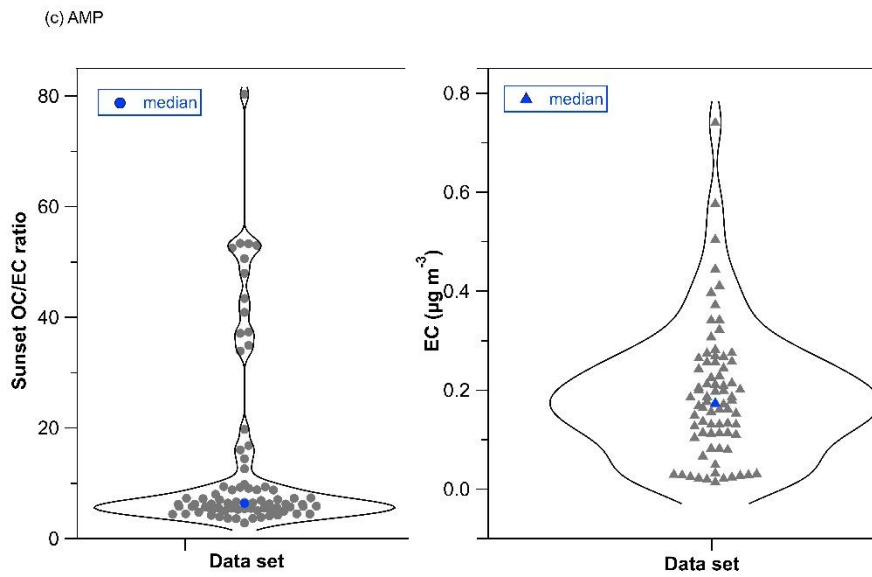
(d) SPP

Figure 9. Violin plots of the OC/EC ratios and EC concentrations for (a) before the monsoon period (BMP), (b) transition monsoon period (TMP), (c) after the monsoon period (AMP), and (d) ship pollution period (SPP) based on the data from the Sunset OC/EC analyzer. The blue solid circles and triangles indicate median values of Sunset OC/EC ratios and EC mass concentrations,

56

1017 **respectively. The total data points are 551 in the data set, with a concentration range of 0.76-7.90 μg m⁻³ for OC and 0.013-22.84 for**

1018 **EC μg m⁻³. Particularly, all OC data is above LOD of 0.18 μg m⁻³ while 29% of EC data is below LOD of 0.19 μg m⁻³.**

1019 ~~Figure 9. Box and whisker plots of the OC/EC ratio vs the EC concentration for (a) before the monsoon period (BMP), (b) transition~~

1020 ~~monsoon period (TMP), (c) after the monsoon period (AMP), and (d) ship pollution period (SPP) based on the data from the Sunset~~

1021 ~~OC/EC analyzer. The whisker top, box top, box bottom, and whisker bottom are 90%, 75%, 25% and 10%, respectively.~~

1022

1023
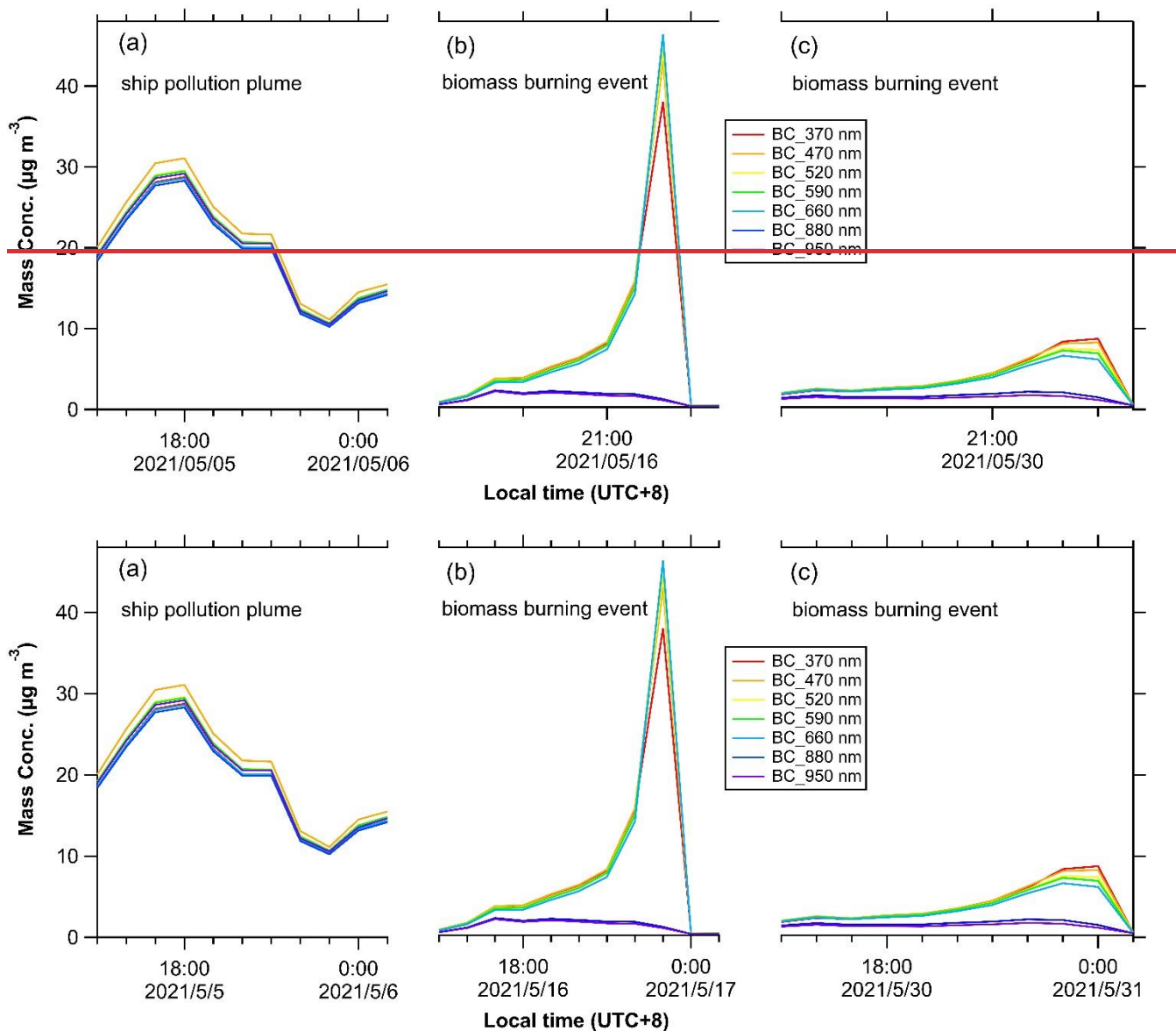
1026 ~~Figure 10. The wavelength-dependent mass concentration from AE33 aethalometer for example spectra for (a) example of a ship~~

1027 ~~pollution plume, and (b, c) two significant biomass burning events during this campaign.~~
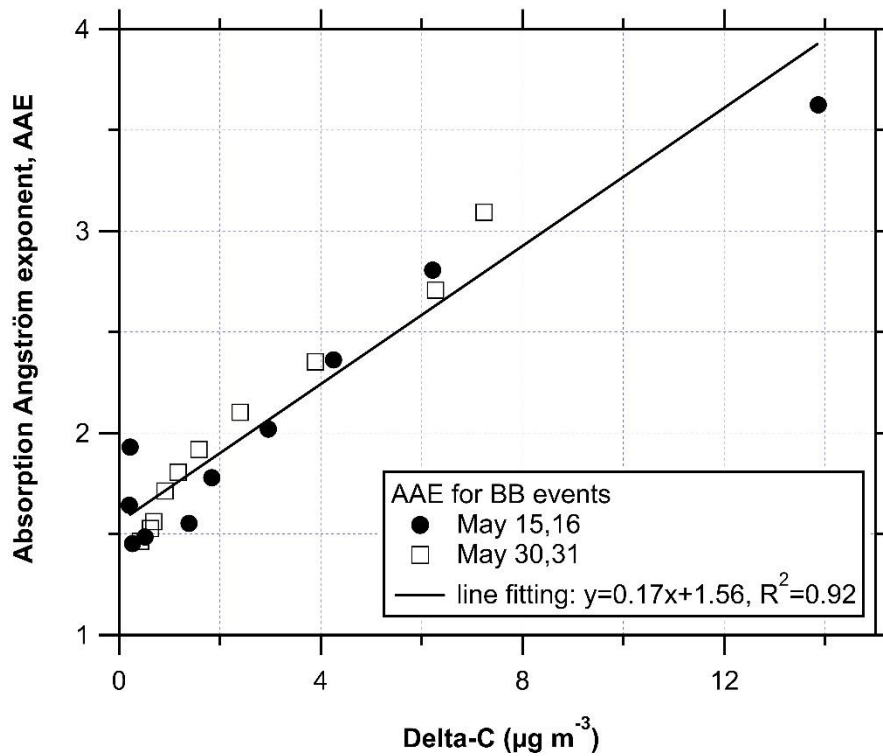
1028

1029

1030
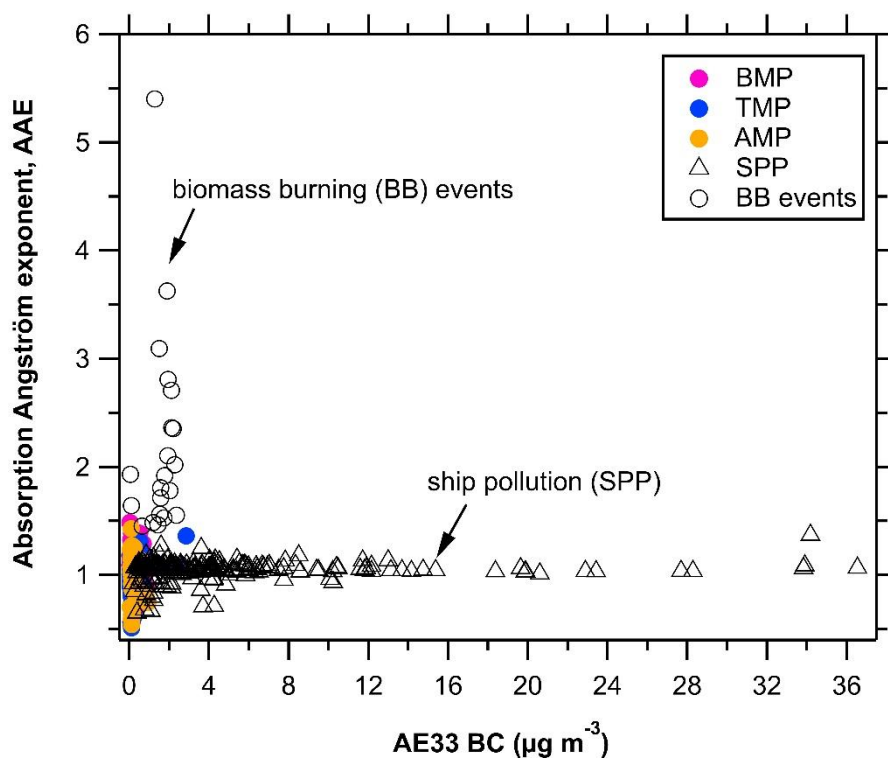
1031

1032 **Figure 11. The absorption Angström exponent (AAE, all wavelengths) vs AE33 BC concentration for before monsoon period (BMP),**

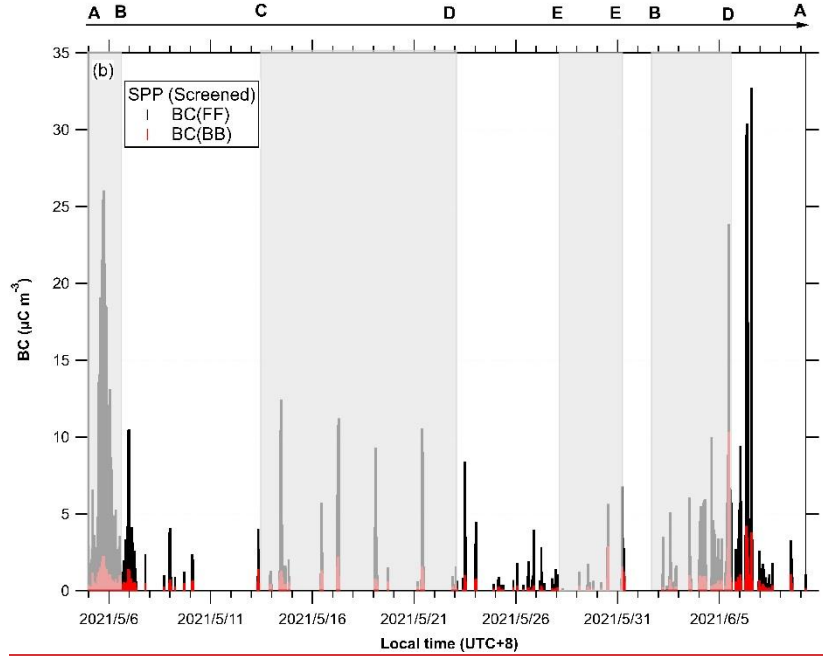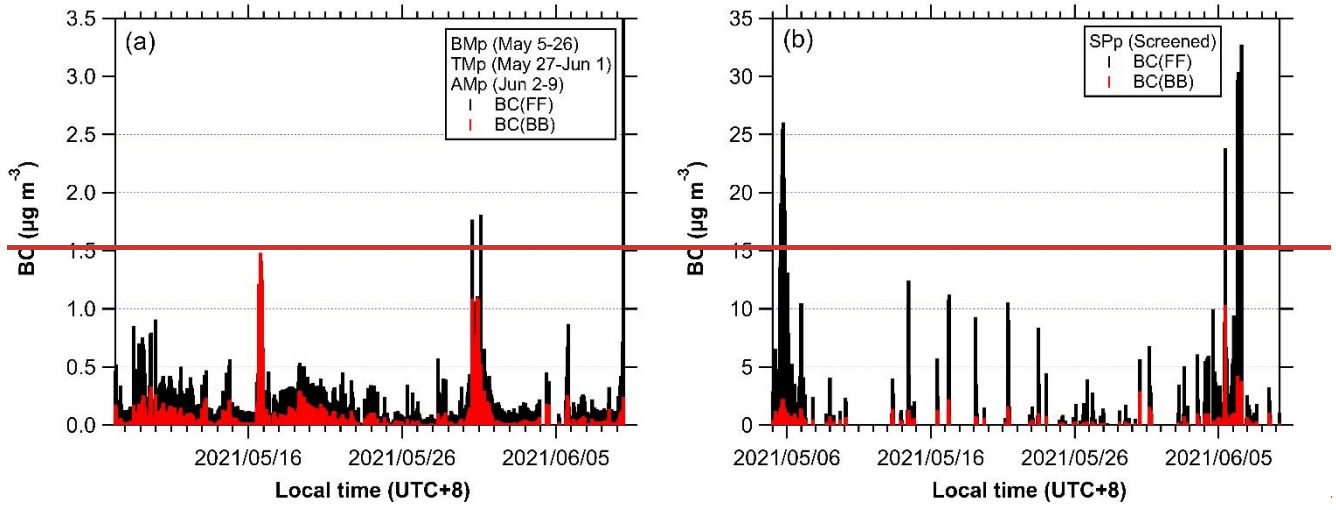1033 **transition monsoon period (TMP), after monsoon period (AMP), and ship pollution period (SPP).**
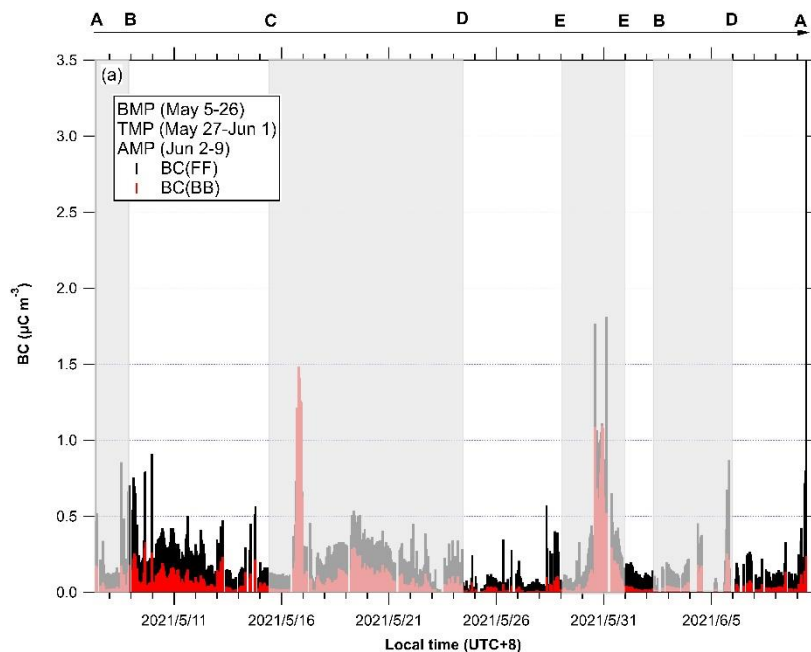
1034

58

Figure 12. The absorption Angström exponent (AAE) vs the Delta-C concentration for the two biomass burning events: BB-1 at

6:00–7:00 on May 15 and 15:00–22:00 on May 16 during BMP, and BB-2 at 15:00-23:00 on May 30 and 00:00 on May 31 during

TMP. The BB-1 and BB-2 data points are marked in solid circles and open squares, respectively.

1039

Figure 13. Source apportionment of the BC particles using the two-component AAE model (AAE=1 for foil fuel (FF) and AAE=2 for biomass burning (BB): (a) before monsoon period (BMP), transition monsoon period (TMP), after monsoon period (AMP), and (b) ship pollution period (SPP). The shaded and unshaded areas sequentially indicate the cruise routes from AB, B to C, C to D, D to E, E to E (ship stop), E to B, B to D, and D to A, as marked in Figure 1.

~~Figure 13. Source apportionment of the BC particles using the two~~ two-component AAE model (AAE=1 for foil fuel (FF) and ~~AAE=2 for biomass burning (BB): (a) before monsoon period (BMP), transition monsoon period (TMP), after monsoon period (AMP), and (b) ship pollution period (SPP).~~